FINAL TECHNICAL REPORT

1 September 1992 - 31 August 1994

Name of Contractor:	California Institute of Technology
Effective Date of Contract:	1 September 1992
Contract Expiration Date:	31 August 1994
Contract Number:	F49620-92-J-0470
Principal Investigator:	Donald V. Helmberger (818)395-6998
Program Manager:	Dr. Stanley K. Dickinson
Short Title of Work:	Mapping Crust and Upper Mantle Structure Beneath Southern Eurasia

Sponsored by
AFOSR/NL
110 Duncan Avenue, Suite B115
Bolling AFB DC 20332-0001
Contract #F49620-92-J-0470

Seismological Laboratory
Division of Geological and Planetary Sciences
California Institute of Technology
Pasadena, California 91125

Summary

Last year's report discusses a back-projection algorithm for inverting P_n travel times to image the lower crust and upper mantle. It was applied to a large set of data observed around the flanks of Tibet. A similar application of this method is given in **Section A** (*Lateral Variations and Azimuthal Isotropy of P_n Velocities beneath the Basin and Range Province*).

Section B (*Lateral Variation in Crustal Structure of the Northern Tibetan Plateau Inferred from Teleseismic Receiver functions*) discusses data observed in the interior of Tibet of teleseismic events.

Section C (*Regional Earthquake Waveform Modeling on the Tibetan Plateau)* treats the problem of inverting broadband data to obtain estimates of both the structure and regional source.

REPORT DOCUMENTATION PAGE

Form Approved
OMB No. 0704-0188

1. AGENCY USE ONLY (Leave blank)	2. REPORT DATE	3. REPORT TYPE AND DATES COVERED
	9 January 1995	FINAL TECHNICAL REPORT 1/9/92-31/8/94

4. TITLE AND SUBTITLE
Mapping Crust and Upper Mantle Structure Beneath Southern Eurasia

5. FUNDING NUMBERS
Contract #F49620-92-J-0470

6. AUTHOR(S)
Donald V. Helmberger

AFOSR-TR- 95 0040

7. PERFORMING ORGANIZATION NAME(S) AND ADDRESS(ES)
Seismological Laboratory
Division of Geological and Planetary Sciences
California Institute of Technology
Pasadena, CA 91125

8. PERFORMING ORGANIZATION REPORT NUMBER
F49620-92-J-0470

9. SPONSORING/MONITORING AGENCY NAME(S) AND ADDRESS(ES)
AFOSR/NL
110 Duncan Avenue, Suite B115
Bolling AFB, DC 20332-0001

10. SPONSORING/MONITORING AGENCY REPORT NUMBER

11. SUPPLEMENTARY NOTES

12a. DISTRIBUTION/AVAILABILITY STATEMENT

12b. DISTRIBUTION CODE

13. ABSTRACT (Maximum 200 words)

Most earthquakes occurring in Southern Asia are apparently caused by the continental collision involving the India and Eurasia plates. Major strike-slip faults have allowed stable portions of Asia to move laterally to accommodate this changing stress field and have contributed to the broad zone of tectonic activity. In this report, we focus on the Tibetan Plateau, its tectonic activity and its velocity structure, since this information is crucial to understanding the above process. In particular, we study the high quality broadband waveforms obtained from the 1991-92 Pascal recording experiment.

About 50 regional events were recorded in epicentral distances less than 1000 km during the experiment. We selected 5 events located in north-central plateau. From a profile naturely formed by one of the events, we can measure the Pn and Sn arrivals and estimate the Pn and Sn velocities to be 8.1 km/s and 4.7 km/s. Several previous velocity models of Tibet are tested by whole waveform modeling and a new model developed where ratios of P to S are obtained (1.8). These ratios are higher than normal, indicative of high temperature in the lower crust. Synthetics generated from this model fit the observed waveforms quite well, especially the SH components. Two kinds of source mechanisms strike-slip and normal faulting, are obtained from a direct grid search procedure from the larger events. These source mechanisms and their indicated stresses support the previous study on the EW extrusion and extension of the crust in the high plateau under the indentation of Indian subcontinent.

14. SUBJECT TERMS			15. NUMBER OF PAGES 1
			16. PRICE CODE
17. SECURITY CLASSIFICATION OF REPORT	18. SECURITY CLASSIFICATION OF THIS PAGE	19. SECURITY CLASSIFICATION OF ABSTRACT	20. LIMITATION OF ABSTR.
Unclassified			Unlimited

Lateral Variations and Azimuthal Isotropy of P_n Velocities beneath Basin and Range Province

Lian-She Zhao

Seismological Laboratory 252-21

California Institute of Technology

Pasadena, CA 91125

Abstract

Travel-time tomography was used to obtain the lateral variations in P_n velocities and P_n velocity azimuthal anisotropy beneath the Basin and Range Province. We used 1226 P_n arrivals from 184 earthquakes recorded by 113 stations. The tomographic image shows the lateral variation in P_n velocity from 7.9 km/s in the northern Province to 7.6 km/s in the southern Province. Azimuthal variations in P_n velocities are less than one percent as determined from the travel time residuals after taking out the contribution of the lateral velocity variations of the P_n tomography. Although the standard errors of the azimuthal variations are about two percent, there is no reason to believe the existence of the P_n azimuthal anisotropy in the uppermost mantle beneath the Basin and Range Province. Beghoul and Barazangi's (1990) suggestion of more than three percent azimuthal anisotropy is the result of the lateral heterogeneity and mantle velocity gradient. Before tomographic inversion, we refined the P_n travel times by considering the lateral variations in the crustal thickness and velocities in the region based on the numerical experiment and theoretical development given in this paper. These refinements are crucial in obtaining an accurate velocity image. The average velocity is 7.72 ± 0.16 km/sec, and an average vertical mantle velocity gradient is 8.0×10^{-4} s^{-1}. The resolution for P_n velocity image is generally within two to five degrees.

Introduction

Anisotropy, a characteristics of many mantle minerals, is important to seismology, since it is responsible for the large variations in seismic velocities. Some researchers have suggested seismic velocity variations due to anisotropy are potentially much greater than those due to other effects such as composition and temperature. Thus, it is

necessary to understand seismic anisotropy well before one attempts to infer chemical, mineralogical and temperature variations from seismic data [*e. g.*, Anderson, 1989]. However, some evidences of the existence of seismic anisotropy can be interpreted as the lateral heterogeneity of the structure, since there is often a direct trade-off between anisotropy and heterogeneity. In order to circumvent this problem, we present a method of identifying P_n velocity azimuthal anisotropy in the presence of the lateral heterogeneity of the crustal and upper mantle.

An anisotropic upper mantle would be expected if it is olivine rich [e. g., Duffy and Anderson, 1989; p. 306, Anderson, 1989]. Crystal alignment may be caused by the motions in the mantle associated with mantle convection, internal deformation of the lithosphere, the preferred local stress field orientation, or recrystallization. Thus, attempts at finding evidence of seismic anisotropy are largely focused on tectonically active regions in the world. Due to limited data and complexity of the Earth, especially in tectonically active regions, it is difficult to identify anisotropy unambiguously in the presence of structural heterogeneity. In order to minimize the contribution of heterogeneity, researchers have turned to shear wave splitting to try to find anisotropy, [*e. g.*, Savage *et al.* 1990; Silver and Chan, 1988, 1991; Xie, 1992]. Numerical experiments show that coupled mode waveform anomalies of surface waves in the frequency range of 0-20 mHz can be diagnostic of upper mantle azimuthal anisotropy [Park and Yu, 1992; Tanimoto and Anderson, 1985; Yu and Park, 1992].

P_n travel times have been used to find evidence for the existence of azimuthal anisotropy [*e. g.*, Bamford *et al.*, 1979; Beghoul and Barazangi, 1990; Hess, 1964; Rait et al., 1971; Vetter and Minster, 1981]. For the Basin and Range province, Beghoul and Barazangi [1990] suggested a 3.2 percent azimuthal anisotropy in P_n velocity. In this study, we rigorously examine P_n velocities beneath the Basin and Range province. We used all possible ISC P_n travel times from 1964 to 1990. We account for the three dimensional local crustal and mantle velocity structure (including

the topography of the surface and the Moho) to refine the apparent P_n velocities before inversion employing the numerical method discussed in detail later. After tomographic inversion, we allocated the non-diminished P_n travel time residuals back to the vertical travel times of the source and receiver. This process is actually the source relocation and local velocity structure refinement. After this process, we obtain a new data set of apparent P_n velocities. We then invert the new data set and allocate the non-diminished residuals after inversion again until the allocation so small that the results of the last two iterations are almost the same. In this study we used four iterations. After the whole process is done, we assume that the non-diminished P_n travel times residuals are mainly due to the azimuthal velocity dependence, since the contribution of lateral variation of the P_n velocities are taken out by the tomographic inversion. Thus, we can find out if P_n velocity residuals calculated from travel time residuals depend on azimuth.

Data

Using the ISC database, we collected 1226 P_n travel times from 184 earthquakes (M_L >2.9) that occurred in or around the Basin and Range province from 1964 to 1990, recorded at 113 stations. The ray paths are shown in Figure 1. We selected paths for which the apparent P_n velocity is between 7.0 - 8.5 km/sec, after correcting the average crustal thickness of 35 km [Braile *et al.*, 1989]. The distance range is 2-11 degrees.

Method and Procedure

We begin with the observed P_n travel times, t_{obs}, which can be written as:

$$t_{obs} = \alpha + \beta + \gamma + \int_s^r S\,dl, \qquad (1)$$

where α is the vertical travel time from source to Moho, β is that from Moho to

receiver, and γ is the contribution of the vertical velocity gradient of the mantle. The horizontal travel time, $\int_s^r Sdl$ is from source, s, to receiver, r, where S is local slowness. In the following, we give a detailed description how to estimate α, β, and γ.

Two dimensional crustal velocity structure

In a crustal structure with weak heterogeneity, α and β can be written approximately as:

$$\alpha = \sum_{j=1}^{j=n_s} \eta_j H_j, \quad \text{and} \quad \beta = \sum_{i=1}^{i=n_r} \eta_i H_i, \tag{2}$$

where n_s and n_r are the numbers of layers beneath the source and the receiver to the local Moho, respectively. H_j is the layer thickness beneath the source, while H_i is the layer thickness beneath the receiver, $\eta_i = (1/v_i^2 - p^2)^{1/2}$ is vertical slowness, where v_i is velocity, and p is ray parameter. α is calculated from the velocity structure close to the source, and β is from the structure close to the receiver (the topography of the surface can be easily included).

We can show the validity of Eq. (2) by comparing with finite difference synthetic seismograms (Vidale et al., 1985). Figure 2 gives a two dimensional model, for which the crustal thickness varies from 50 km to 30 km. Figure 3 gives the finite difference synthetics of the model (solid lines, which are truncated seismograms), predictions of Eq. (2) (arrows) , and picks (with 0.1 seconds error bar) from the synthetics (solid dots). The maximum difference between picked and calculated travel times is 0.3 seconds, which contrast greatly with the more than one second difference in the reduced travel times for all traces. Assuming the model at the source end is the model for the whole path, we have a reduced travel time of 7.9 seconds. In contrast, the reduced travel time is only 4.6 seconds if using the model at 200 km from the source as the model for the whole path. Thus, Eq. (1) is a good approximation for

the head travel times in two dimensional velocity structures. If the crustal velocity structure does not change very rapidly in a few tens of kilometers (order of the crustal thickness) in horizontal direction, the error of the predictions of Eq. (2) is very small (see the 210-270 km and 360-470 km ranges of Figures 2 and 3).

The model used to estimate α is the model at 50 km from the source, roughly the distance from the source to Moho. For β, the model used is at 40 km to the receiver. If the velocity structure is roughly the same in a few tens of kilometers in the horizontal direction, which is not true for the model given in Figure 2, we can use the velocity structure below the source and receiver to estimate α and β of Eq. (2).

The absolute travel times of finite difference synthetic seismograms are refined by comparing the finite difference results of an averaged one-dimensional model of the a two-dimensional model used (Figure 2). For one-dimensional models, the head wave travel times can be calculated analytically. The highest frequency end of the synthetics is one Hertz. In the complex structures, the picked P_n time may not be the minimum travel time for the model, because the energy of the phase may be too small to be noticed.

The good approximation of Eqs.(1) and (2) can be understood theoretically. The head waves travel almost horizontally in the mantle so that the horizontal travel time would be approximately the integral in Eq. (1). The head wave travel time would be the minimum travel time, so the ray has the critical angle incidence to the local Moho at the source and leaves the local Moho at the critical angle to go to the receiver. Eq.(1) is a good approximation as long as the structure is sufficiently close to one-dimensional, since the ray parameter P is no longer a constant in two-dimensional velocity structures.

A constant velocity gradient mantle

If a mantle has a constant velocity gradient, then the travel times of head waves

are not a linear function of distance. If we use the form

$$v = v_0(1 + cz) \tag{3}$$

to represent the velocities in the mantle, where z is the depth from Moho (downward is positive), c is a constant whose product with v_0 gives the mantle velocity gradient for a flat Earth. For a spherical Earth, the velocity gradient is $(c - 1.58 \times 10^{-4}) v_0$ when the units for c and v_0 are km^{-1} and km/s, respectively [Helmberger, 1973]. The observed head wave velocity is $v_{obs} = X / t$, where X is the horizontal distance in the mantle, and t is the minimum travel time of the model at this distance (we used v_{obs} here because its definition is the same as that used to estimate the average observed velocity for head waves, and to show the difference from the conventionally used head wave velocity of v_0). v_{obs} can be written as

$$v_{obs} \approx v_0 + \frac{c^2}{24} v_0 X^2, \tag{4}$$

when $c \ll 1$, which is usually holds for the real Earth. Eq. (4) is valid when $X < X_m = ((1 + cH_m)^2 - 1)^{1/2} / c$, where H_m is the maximum depth that Equation (3) holds. When $X > X_m$, we have

$$v_{obs} \approx v_0 + v_0 c H_m (1 - \frac{2X_m}{3X}) \tag{5}$$

The derivations of Eqs. (4) and (5) are given in the Appendix.

From Eqs. (4) and (5), γ in Eq. (1) can be written as

$$\gamma \approx - \frac{X}{v_0} \frac{\delta v}{v_0}, \tag{6}$$

where δv is the second term in Eqs. (4) or (5).

Inversion method

Once α and β are calculated from Eq. (2) and the local velocity structure is removed from t_{obs} in Eq. (1), we have

$$v_{obs} = D/(t_{obs} - \alpha' - \beta') \quad \text{and} \quad X = D - A - B, \tag{7}$$

where D is the horizontal source-receiver distance, the primed quantities are estimated ones from available information. A and B, the horizontal travel distances of the P_n ray in the crust beneath the source and receiver, can be estimated from local crustal model. For every path, once v_{obs} and X are determined, we can calculate c from Eqs. (4) and (5) using the least squared method, and then γ from Eq. (6).

For each of (i , j), source i to receiver j, we have:

$$(\int_s^r S\, dl)_{ij} = \sum_k^k \Delta_{ijk} s_k = (t_{obs})_{ij} - \alpha'_i - \beta'_j - \gamma'_{ij} - RES_{ij}, \tag{8}$$

where Δ_{ijk} is the length of the line segment over which the (i,j)th path overlaps the kth grid, s_k is the slowness in the kth grid, and the travel time residual for (i, j) path is

$$RES_{ij} = \delta\alpha_i + \delta\beta_j + \delta\gamma_{ij}$$

$$= (\alpha_i - \alpha'_i) + (\beta_j - \beta'_j) + (\gamma_{ij} - \gamma'_{ij}) .$$

Then Eq. (8) can be rewritten as

$$\sum_k^k \Delta_{ijk} s_k + RES_{ij} = (t_{obs})_{ij} - \alpha'_i - \beta'_j - \gamma'_{ij}. \tag{9}$$

The right side of Eq. (9) is known. This equation forms a standard linear inverse problem for unknown s_k. We used a back-projection, or SIRT algorithm (e. g. Humphreys and Clayton, 1998; Xie and Mitchell, 1990) to solve for s_k. In particular, we use the 9-grid smoothing operation (Suetsugu and Nakanishi, 1985; Xie and Mitchell, 1990) between iterations. This operation is used to overcome insufficient spatial data coverage, at a slight cost to resolution.

Method to refine α and β

In the back-projection calculation, s_k values are updated during the iterations to reduce the misfit of left and right side of Eq. (9). When the misfit stops decreasing,

we end up with with the final slowness model (values of s_k) and some non-diminished RES_{ij} values. To the first order approximation we assume that RES_{ij} are dominatedly caused by imprecise estimates on α_i and β_j; we then have

$$RES_{ij} \approx \delta\alpha_i + \delta\beta_j. \tag{10}$$

Non-zero $\delta\alpha$ are primarily due to the mislocation of the source (location, depth, and origin time), and the erroneous crustal structure used before the inversion, and non-zero $\delta\beta$ is purely from erroneous crustal structure. Eq. (10) also forms a linear inversion problem, for which we used the least square method to allocate RES_{ij} back to α_i and β_j. This means that the sources are relocated and the local crustal models for the source and receiver regions have been improved in the new slowness model.

After new α_i and β_j are determined, we implement the back-projection again to update s_k model, then update α and β again, until the maximum of the allocations $\delta\alpha$ and $\delta\beta$ of α and β reaches some small limit.

Method of estimating azimuthal anisotropy

Since the velocity image (s_k model) is an average in all directions, it is reasonable to assume that the non-zero travel time residuals, RES_{ij}, result mainly from the possible azimuthal anisotropy, after all inversion process in the earlier sections is done. We define the velocity residual as:

$$\frac{\delta v}{v} = \frac{v_{obs} - v_{syn}}{v_{syn}} = \frac{RES}{t_{obs} - \alpha - \beta - \gamma}. \tag{11}$$

For one particular azimuth θ, we use average

$$\left(\frac{\delta v}{v}\right)_{av} = \frac{\sum_{\theta-10}^{\theta+10} \left(6 - \frac{|\theta_i - \theta|}{2}\right)\left(\frac{\delta v}{v}\right)_i}{\sum_{\theta-10}^{\theta+10} \left(6 - \frac{|\theta_i - \theta|}{2}\right)} \tag{12}$$

as the velocity residuals at this azimuth, where i is the path within the 20 degree

interval. And we use the square root of

$$\frac{\sum_{\theta-10}^{\theta+10}(6-\frac{|\theta_i-\theta|}{2})((\frac{\delta v}{v})_i-(\frac{\delta v}{v})_{av})^2}{\sum_{\theta-10}^{\theta+10}(6-\frac{|\theta_i-\theta|}{2})} \qquad (13)$$

as the standard deviation of this velocity residual.

Results

We used the resulting models of seismic sounding studies [Braile et al., 1989] as local models to estimate α and β, and obtained α' , β' values for the source and the receiver delays, calculated from Eq. (2). In this estimation, we assumed that the velocity structure does not vary rapidly. The topography of the surface of the Earth is included.

Mantle velocity gradient

Using Burdick and Helmberger's [1978] T7 model, which was proposed for the western United States, we can get an estimate for X_m of 2400 km, much greater than the maximum distance we used in this study. Thus, we can use Eqs. (4) and (7) to estimate c, and obtain $c = 2.56 \times 10^{-4}$, which is the average for all ray paths, and mantle velocity gradient $2.0 \times 10^{-3} s^{-1}$, including the contribution of the Earth's sphericity $1.2 \times 10^{-3} s^{-1}$. γ' can be estimated by using Eq. (6). At a distance of 1200 km, γ' is -0.6 seconds.

P_n velocity image

After accounting for α', β' and γ', we used four allocation iterations to find solutions for Eqs. (9) and (10) so that the maximum of $\delta\alpha$ and $\delta\beta$ was less than 0.2 seconds. We divide the area between 29° -47°N and 107°-126°W into 1406 blocks of a size of $0.5° \times 0.5°$. Figure 4 gives the final velocity image. The average velocity of

this image is 7.72 ±0.16 km/s. (The P_n velocities are given at depth of 30 km.) The velocity image shows a faster velocity in the north and a slower velocity in the south (Figure 4). The slow velocity regions in the uppermost mantle beneath Sierra Madre and the southern end of Nevada appear to be connected.

Along the Sierra Nevada, the P_n velocity is less than 7.7 km/sec, which agrees well with the velocity 7.6-7.65 km/s of Jones *et al.* [1992], 7.6-7.7 km/s of Hearn et al. [1991].

The slow P_n velocities in the southern Basin and Range province (Figure 4) are compatible with Biasi and Humphreys' [1992] velocity image of depth range 30-60 km. However, they obtained a faster region at the northwest of Southwest Nevada Volcanic Field (roughly at 38°N, 117°W) closer to the Nevada boundary than this study. The reason for this is probably that the mantle velocity gradient is larger beneath that region. Hearn et al. [1991] also found a slow region in the south, albeit a much smaller one, which may be because of the flat Moho assumption used in their study. We will return to this later.

Azimuthal anisotropy

The analysis of the travel time residuals, after the inversion and allocation procedure is done, is given in Figure 5, in five degree spacing, using Eqs. (12) and (13). The denominators, $\sum_{\theta-10}^{\theta+10}(6 - |\theta_i - \theta|/2)$, in Eqs. (12) and (13) are given in Table 1. The value of the denominator at one azimuth represents the number of P_n travel time picks in a 20 degree azimuthal interval centered at the azimuth. The average is 241.1, roughly equivalent to 70 picks in 20 degree intervals. None of the average velocity residuals exceeds one percent (Figure 5). The average velocity residuals at azimuth 80°- 100° are about 0.9 percent. However, the denominator values for their 20 degree interval are less than half of the average (Table 1). The error bars are mostly larger than two percent. Thus, the azimuthal anisotropy in P_n velocity, if any, is not likely to

be greater than one percent for the Basin and Range province.

Error analysis and resolution of the P_n velocity image

In this section, we quantitatively assess the quality of the two-dimensional P_n velocity image obtained in this study. We also present the P_n velocity images, (1) without correcting for a mantle velocity gradient and (2) assuming a homogeneous crust and mantle.

In tomography, the spatial resolution at a given grid can be approximated by the point spreading function (p.s.f.) calculated for the grid, *e. g.*, Humphreys and Clayton, 1988; Xie and Mitchell, 1990. We calculated the p.s.f. for six grids, five close to the boundaries, one in the center of the region (Figure 6a). We put three grids of the p.s.f. on one plot, since they do not overlap each other. The spatial resolution is generally less than 3 degrees, and less than 2 degrees at locations where the ray coverage is more dense. However the grid beneath Sierra Nevada (the lower dark one of Figure 6a) spreads about five degrees. This is caused by parallel rays passing through most of area. However, point spreading function gives only the resolution that can be achieved from the given ray path coverage.

Figure 7 gives the velocity image without correcting for mantle velocity gradient, that is, $\gamma' = 0.0$. The average velocity is 7.73 $\pm$0.16 km/sec. The main pattern of the velocity distribution of Figure 7 is about same as that of Figure 4. However, the slower P_n velocity regions in the south are smaller and not connected to each other in Figure 7, as compared with that in Figure 4. The small difference in Figures 4 and 7 is due to small positive mantle velocity gradient, $2.0 \times 10^{-3} s^{-1}$.

As has been discussed before, we used the crustal and upper mantle velocity models of seismic sounding studies to estimate α' and β' from Eq. (2). In this section, we show the results from the assumption of a homogeneous uppermost mantle velocity model, which is an average model of the Basin and Range province [Braile et

al., 1989], with a compressional velocity of 6.25 km/s for the crust and 7.8 km/s for the mantle, and with a thickness of 35 km, for the whole Basin and Range province. The α' and β' values estimated also from Eq. (2). The velocity image is given in Figure 8. The average P_n velocity of 7.77 $\pm$0.16 km/s in Figure 8 is higher than that of 7.72 km/s in Figure 4. The main features of the velocity distribution are similar except for the southern end, at which the P_n velocities are much exaggerated. The slow regions are reduced beneath the Sierra Nevada and southern Nevada (Figures 4 and 8). The fast regions are expanded, for example, see northern portion of the study area. The southern end of the study area, close to the Gulf of California, P_n velocities becomes fast (Figure 8), which is very similar to the results of Hearn et al. [1991]. The actual crustal thickness in the region of th south end is about 25 km [Braile et al., 1989], 10 km thinner than that was used. Thus, α' or β' is about one second greater than α and β, the travel time is smaller for any ray ending within this region.

Error analysis of azimuthal anisotropy

The azimuthal velocity residuals plotted in Figure 9 are calculated the P_n velocity image given in Figure 7, without correcting the mantle velocity gradient. The averaged values are almost identical to that derived from a model with a positive velocity gradient mantle. This implies that the assumption of a homogeneous mantle does not effect the velocity residual dependence on azimuth. However, the two station method of Beghoul and Barazangi [1990] tends to enlarge the contribution of the mantle velocity gradient to the velocity residuals. For example, the P_n velocities from the two station method are 7.82 km/s for distance of 500 km (two stations at 1000 and 1500 km) and 7.73 km/s for distance of 300 km (two stations at 200 and 500 km) instead of the real velocity of 7.72 (200 km) and 7.73(500 km), using v_0 7.72 km/s and c 2.56 $\times 10^{-4} s^{-1}$ obtained previously. The correction of the average mantle velocity gradient should not affect the azimuthal anisotropy, since the correction is the

same in every direction.

Assuming a homogeneous model for both crust and mantle, we obtained the velocity image given in Figure 8, the azimuthal velocity residuals of which are given in Figure 10. The similarity of Figure 5 to Figure 10 infers that the initial crustal models do not effect the azimuthal dependence of the velocity residuals. Note that the contributions of the lateral variation of the P_n velocities, the mislocation of the events, and lateral variation of the crustal structure to the azimuthal P_n velocity residuals were taken out in the course of inversion and allocation procedure.

We use the refined P_n travel time data set, which is not yet put through the last inversion to get the tomographic image in Figure 8. This means that the lateral variations in the P_n velocities is put back to the travel times, and the α and β values are refined. The average velocity of 7.77 $\pm$0.16 km/s was given above for this data set (Figure 8). We use this values as the velocity for the upper mantle beneath the whole studied area (homogeneous). The azimuthal velocity residuals are given in Figure 11. The fluctuation of the averaged velocity residuals is larger than the residuals shown in Figure 5.

Figure 12 gives the azimuthal velocity residuals for the raw data with correcting a homogeneous crust and upper mantle. The average velocity is 7.77 $\pm$0.20 km/sec. The standard error is larger than that in Figure 11. The pattern of Figure 12 is roughly the same as that of Figure 11. This figure suggests that as long as the ray paths are dense there is no evidence for azimuthal anisotropy in the Basin and Range province, regardless of the assumptions made in the crustal and mantle velocity structures.

Discussion and conclusions

P_n velocity image

The inversion method and procedure used in this study to get the P_n velocity image differ from those in previous P_n tomography studies, for example, Hearn et al. [1991]. We used the following two steps prior to the back projection inversion:

(1) We estimated the vertical travel times for the sources and receivers, with a priori knowledge on the lateral variation of in crustal structure. These delay times were then subtracted from the P_n travel times to obtain the apparent P_n velocity.

(2) We estimated the average mantle velocity gradient, which was used to correct the apparent P_n velocities to get P velocities along the uppermost mantle.

The numerical experiment and theoretical development that make these two corrections possible are given in this study.

The average P_n velocity from the inversion is 7.72 ± 0.16 km/sec. The average mantle velocity gradient obtained in this study is $2.0 \times 10^{-3} s^{-1}$, including the contribution of the Earth's sphericity, $1.2 \times 10^{-3} s^{-1}$. Two distinct low P_n velocity regions beneath the Sierra Nevada mountains and southern Nevada seem to be connected and form one large low velocity region in the southern Basin and Range province. The P_n velocity is less than 7.8 km/s in the south; and it is greater than the 7.8 km/s in the north. These slow and fast regions form two big east-west strips (Figure 4). The P_n velocity pattern of low-south and fast-north, in an almost east-west in direction, could be due to upwelling beneath the Sierra Nevada and crustal extension in the southern Nevada, and as discussed above. It may, also, represent a small convection current occurred here in the region, upwelling in the south and downwelling in the north beneath the Basin and Range province, if the velocity differences are caused by the temperature.

The P_n velocity image is not affected much by the mantle velocity gradient. But, the three dimensional crustal structure is crucial to the P_n velocity image. The lower or faster velocity pattern is largely the result of the too short or too long estimates of the station and receiver delay times. The resolution of the velocity image is

generally within three degrees, within two degrees for the grids with denser ray coverage, and within five degrees for poorer ray coverage grids.

Azimuthal anisotropy of P_n velocities

The method used in this study to infer the P_n velocity anisotropy also differs from previous studies, e. g., Vetter and Minster [1981], in the following ways:

(1) Most important of all, we took away the lateral variation in P_n velocities from the possible azimuthal dependence of the velocity residuals, by using tomographic inversion.

(2) Relocation of the sources and refinement of the local crustal structures beneath the sources and receivers.

P_n azimuthal anisotropy for this region, if any, is not likely to be greater than one percent from velocity residuals calculated from various models. However, previous P_n studies suggested more than three percent anisotropy [Vetter and Minster, 1981; Beghoul and Barazangi, 1990]. The obvious reason for this discrepancy is due to the heterogeneity and the much larger volume of the present dataset. An azimuthal dependence might show up if the stations were located within some limited region as the case considered by Vetter and Minster [1981]. For example, all stations are located in the center of the region with earthquakes around them (Figure 8). The seismic anisotropy in this method is merely the lateral variation. The two station method, which was used by Beghoul and Barazangi [1990] to estimate P_n velocities for this region, does not account for the mantle velocity gradient. Mantle velocity gradient and lateral variations of P_n velocities are responsible for the anisotropy in this case.

For the azimuthal velocity residuals, the effects of the mantle velocity gradient and the initial crustal models are small. The lateral variation of the P_n velocities and refinements of the vertical travel times of the sources and receivers are substantial;

they affect both the amplitude and general pattern.

Savage et al., [1990] found favorable evidence of azimuthal anisotropy from shear wave splitting studies. This may suggest that there is no anisotropy a few tens of kilometers beneath Moho, but at greater depths anisotropy appears, since the ray paths for P_n are horizontal while that of SKS are almost vertical. It may also suggest that the mineralogy at the shallow depth beneath Moho has a rich content of some mineral which has a strong shear velocity anisotropy and a weak compressional velocity anisotropy, such as spinel and rutile.

In conclusion, we applied the tomographic inversion method to 1226 P_n travel times from ISC catalogs to study the P_n velocity distribution and anisotropy beneath the Basin and Range province. We obtained a velocity image with slow velocities in the south and fast velocities in the north. The image may suggest a upwelling beneath the Sierra Nevada and a crustal extension beneath southern Nevada. It may also suggest a small convection current occurred beneath this region, with upwelling in the south and downwelling in the north. Before the inversion, we refined the apparent P_n velocities by correcting vertical travel times for sources and receivers using three dimensional crustal structures and correcting for the mantle velocity gradient, which are progressively refined in the course of the inversion and allocation procedure. The aforementioned refining process of the dataset is crucial in obtaining an accurate P_n velocity image, but does not affect the azimuthal dependence of the velocity residuals, although the amplitude of these is increased. Azimuthal anisotropy in the uppermost mantle beneath the Basin and Range province is very small, less than one percent, if present at all, in spite of the strong orientation of the local stress fields.

Acknowledgment

I would like to thank Don L. Anderson for his suggestions, and Robert W. Clayton for showing me how to read his 1964-1986 ISC catalogs. I would also like to thank Don

L. Anderson, James Ni, and Bradley Woods for their review of the manuscript, and Ilya Tsvankin and John Scales for their reviews and comments. This research was supported by the Advanced Research Projects Agency of the Department of Defense and was monitored by the Air Force Geophysical Laboratory under the contract F49620-92-J-0470, Contribution No. 5216, Division of Geological and Planetary Sciences, California Institute of Technology, Pasadena, California.

Appendix

We assume that the mantle velocity is given by Equation (3), i. e.,

$$v(z) = v_0(1 + cz) . \tag{A1}$$

For head waves (such as P_n) turning at a depth, h, the ray parameter is $1/v(h)$, and the travel time $T(h)$ is given by:

$$T(h) = \frac{X}{v(h)} + 2\int_0^h \left(\frac{1}{v(z)^2} - \frac{1}{v(h)^2}\right)^{1/2} dz$$

$$= \frac{1}{v_0(1+ch)}\left[X - \frac{2}{c}((1+ch)^2-1)^{1/2} + \frac{2(1+ch)}{c}\ln(1+ch+((1+ch)^2-1)^{1/2})\right] , \tag{A2}$$

where X is the horizontal distance traveled in the mantle. The head wave travel time over X should satisfy $dT(h)/dh = 0$, we have:

$$X = \frac{2}{c}((1+ch)^2 - 1)^{1/2} , \tag{A3}$$

and the head wave travel time over X is:

$$T = \frac{2}{v_0 c}\ln(1+ch + ((1+ch)^2-1)^{1/2}) . \tag{A4}$$

From definition, The observed head wave velocity is $v_{obs} = X/T$. From (A3) and (A4) we have:

$$v_{obs} \approx v_0 \frac{\sqrt{2ch}\,(1+ch/4)}{ln\,(1+ch+\sqrt{2ch}\,(1+ch/4))} \approx v_0 \frac{\sqrt{2ch}\,(1+ch/4)}{\sqrt{2ch}\,(1-ch/12)} \approx v_0(1+\frac{ch}{3}) , \tag{A5}$$

if $ch \ll 1$. For $ch \ll 1$, X can be approximated by

$$X \approx \sqrt{8h/c} , \quad or \quad h \approx cX^2/8 . \tag{A6}$$

Substituting (A6) into (A5), we have Eq.(4) in the text.

$$v_{obs} \approx v_0(1 + c^2X^2/24) .$$

If $X > X_m = ((1+cH_m^2)-1)^{1/2}/c$, at which the ray bottoms the depth of H_m,

below which Eq.(A1) does not hold, Eq. (A4) should be written as:

$$T = \frac{X - X_m}{v_0(1+cH_m)} + \frac{2}{v_0 c}\ln(1+cH_m + ((1+cH_m^2) - 1)^{1/2})$$

$$\approx \frac{X - X_m}{v_0(1 + cH_m)} + \frac{X_m}{v_0(1 + \frac{1}{3}cH_m)}$$

$$\approx \frac{X + \frac{2}{3}X_m cH_m}{v_0(1 + cH_m)} . \qquad \text{(A7)}$$

From the definition of $v_{obs} = X/T$, we have

$$v_{obs} \approx \frac{1 + \frac{2X_m}{3X}cH_m}{v_0(1 + cH_m)} \approx v_0 + v_0 cH_m(1 - \frac{2X_m}{3X}) ,$$

Eq.(5) in the text.

References

Anderson, D. L., *Theory of the Earth*, Blackwell Scientific Publications, Boston, 1989.

Bamford, D., M. Jentsch, and C. Prodehl, P_n anisotropy studies in northern Britain and the eastern and western United States, *Geophys. J. R. astr. Soc.*, *57*, 397-429, 1979.

Beghoul, N., and M. Barazangi, Azimuthal anisotropy of velocity in the mantle lid beneath the basin and range province, *Nature*, *348*, 536-538, 1990.

Biasi, G. P., and E. D. Humphreys, P-wave image of the upper mantle structure of central California and southern Nevada, *Geophys. Res. Lett.*, *19*, 1161-1164.

Braile, L. W., W. J. Hinze, R. R. B. von Frese, and G. R. Keller, Seismic properties of the crust and uppermost mantle of the conterminous United States and adjacent Canada, in *Geophysical framework of the continental United States* edited by Pakiser, L. C., and W. D. Mooney, Geological Society of America Memoir 172, Boulder, Colorado, 655-679, 1989.

Burdick, L. J., and D. V. Helmberger, The upper mantle P velocity structure of the Western United States,*J. Geophys. Res.*, *83*, 1699-1712, 1978.

Duffy, T. S., and D. L. Anderson, Seismic velocities in mantle minerals and the mineralogy of the upper mantle, *J. Geopys. Res.*, *94*, 1895-1912, 1989.

Hearn, T., N. Beghoul, and M. Barazangi, Tomography of the Western United States from regional arrival times, *Geophys. J. Res.*, *96*, 16369-16381, 1991.

Helmberger, D. V., 1973. Numerical seismograms of long-period body waves from seventeen to forty degrees, *Bull. Seism. Soc. Am.*, **63**, 633-646.

Hess, H., Seismic anisotropy of the uppermost mantle under oceans, *Nature*, *203*, 629-631, 1964.

Humphreys, E., and R. W. Clayton, Adaptation of back projection tomography to se-

ismic travel time problems, *J. Geohys. Res.*, *93*, 1073-1086, 1988.

Jones, C. H., H. Kanamori, and S. W. Roecker, Missing roots and mantle "drips": Regional P_n and teleseismic arrival times in the southern Sierra Nevada and vicinity, California, *J. Geophys. Res.*, in press, 1992.

Park, J., and Y. Yu, Anisotropy and coupled free oscillations: simplified models and surface wave observations, *Geophys. J. Int.*, *110*, 401-420, 1992.

Rait, R. W., G. G. Shor, T. J. G. Francis, and H. H. Kirk, Mantle anisotropy in the Pacific Ocean, *Tectonophysics*, *12*, 1971.

Savage, M. K., P. G. Silver, and R. P. Mayer, Observations of teleseismic shear-wave splitting in the basin and range from portable and permanent stations,*Geophys. Res. Lett.*, *17*, 21-24, 1990.

Silver, P. G., and W. W. Chan, Implications for continental structure and evolution from seismic anisotropy, *Nature*, *335*, 34-39, 1988.

Silver, P. G., and W. W. Chan, Shear-wave splitting and subcontinental mantle deformation, *J. Geophys. Res.*, *96*, 16429-16454, 1991.

Suetsugu, D., and I. Nakanishi, Tomographic inversion and resolution for Rayleigh wave phase velocities in the Pacific Ocean, *J. Phys. Earth*, *33*, 345-368, 1985.

Tanimoto, T., and D. L. Anderson, Lateral heterogeneity and anisotropy of the upper mantle 100-200s, *J. Geophys. Res.*, *90*, 1842-1858, 1985.

Vetter, U., and J. B. Minster, P_n velocity anisotropy in southern California, *Bull. Seis. Soc. Am.*, *71*, 1511-1530, 1981.

Vidale, J. E., D. V. Helmberger, and R. W. Clayton, Finite-difference seismograms for SH waves, *Bull. Seism. Soc. Am.*, *75*, 1765-1782, 1985.

Xie, J., Shear wave splitting near Guam, *Phys. Earth Planet. Int.*, *72*, 211-219, 1992.

Xie, J., and B. J. Mitchell, A back-projection method for imaging large-scale lateral variations of Lg coda Q within application to continental Africa, *Geophys. J. Int.*, *100*, 161-181, 1990.

Yu, Y., and J. Park, Upper mantle anisotropy and coupled-mode long-period surface waves, submitted to *Geophys. J. Int.*, 1992.

Table 1. $\sum_{\theta-10}^{\theta+10}(6-\frac{|\theta_i-\theta|}{2})$

θ	SUM	θ	SUM	θ	SUM
0	452.0	125	203.8	245	221.0
5	449.2	130	223.1	250	174.5
10	335.2	135	232.2	255	136.2
15	318.9	140	226.4	260	124.3
20	395.4	145	177.9	265	93.0
25	394.4	150	183.5	270	74.2
30	339.9	155	278.9	275	70.5
35	311.8	160	358.4	280	94.7
40	311.6	165	375.8	285	145.5
45	282.7	170	319.0	290	168.8
50	224.5	175	243.6	295	180.3
55	192.3	180	228.7	300	200.7
60	195.6	185	265.9	305	251.3
65	186.6	190	316.1	310	324.3
70	136.4	195	316.4	315	326.8
75	90.6	200	331.4	320	268.3
80	103.9	205	371.8	325	234.7
85	122.0	210	342.9	330	218.2
90	115.2	215	284.7	335	196.0
95	112.3	220	279.0	340	181.0
100	128.2	225	319.2	345	182.1
105	184.1	230	320.4	350	215.0
110	220.2	235	285.8	355	324.2
115	210.6	240	255.6	360	452.0
120	190.2				

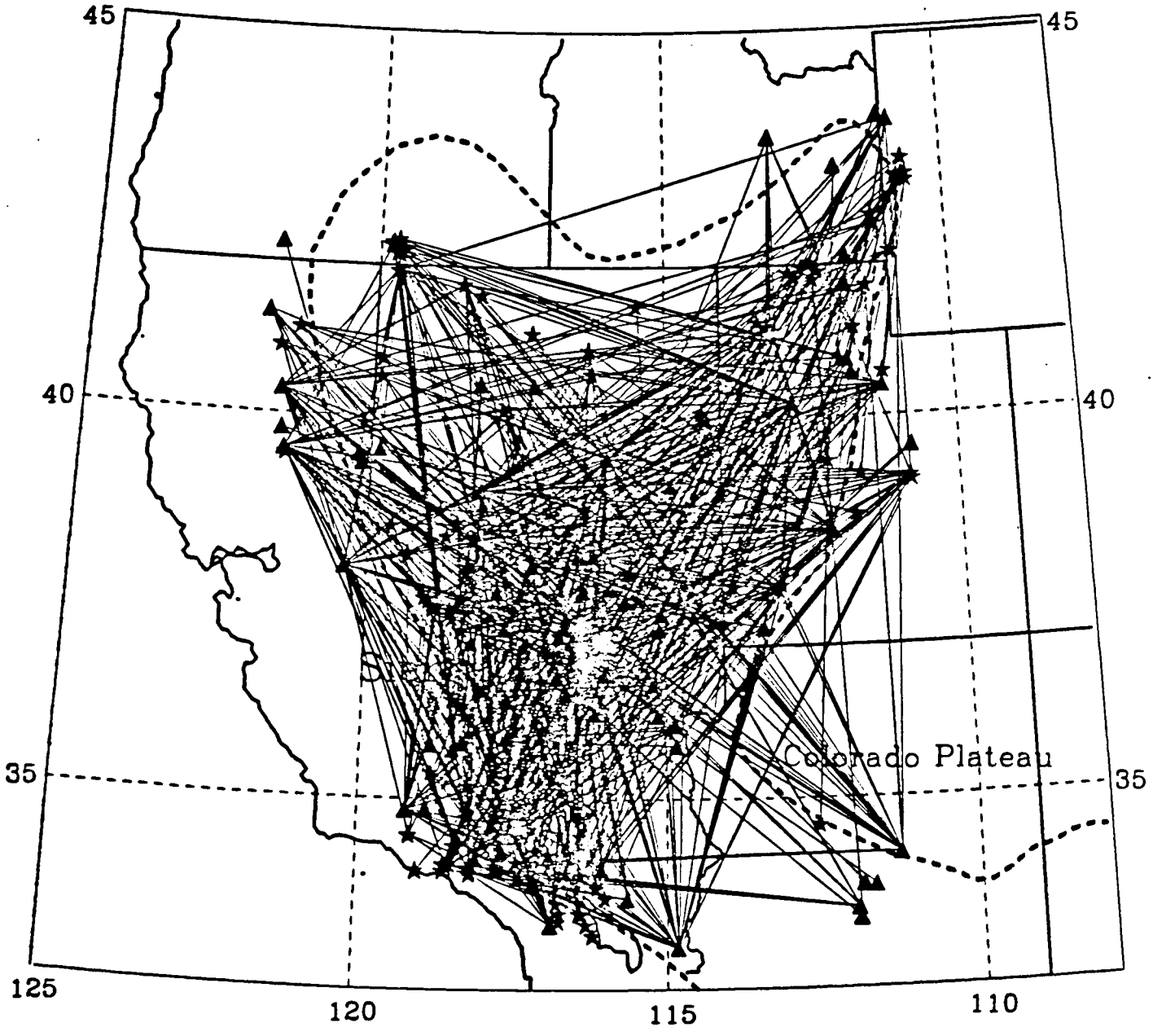

Figure 1. Ray paths. Triangles are stations and stars are earthquakes. Heavy dash lines depict the boundaries of the Basin and Range province. State boundaries are also included.

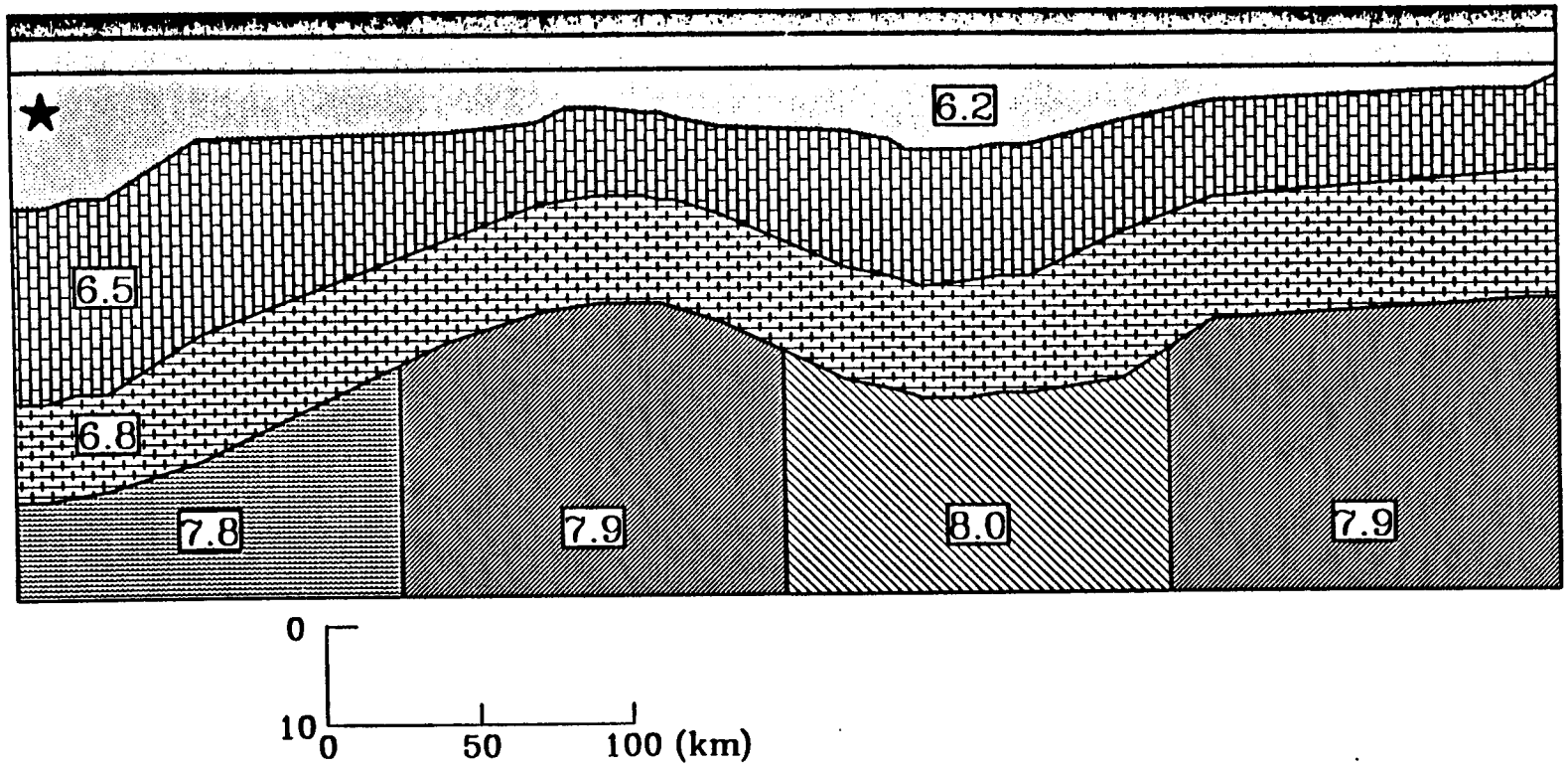

Figure 2. Two dimensional model used to generate finite difference synthetic seismograms. The velocities for blocks are given in the boxes. The velocity is 5.2 km/sec for the layer at the top, for the layer beneath it, the velocity is 6.0 km/sec. The star is the source.

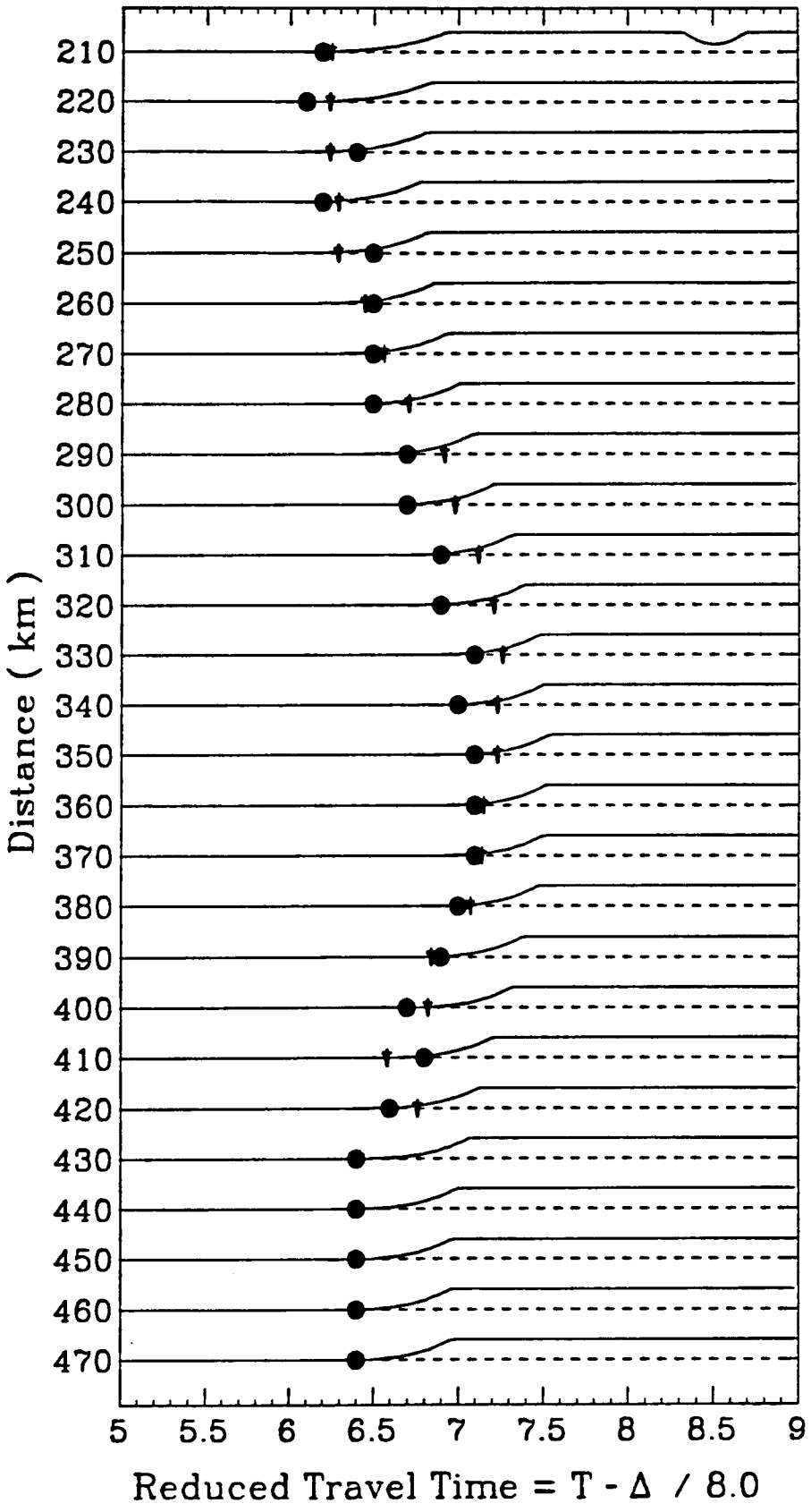

Figure 3. Comparison of the theoretical calculations using Eqs. (1) and (2) with the numerical calculation using finite difference synthetic seismogram method. The solid lines are truncated synthetic seismograms. The solid dots are the travel time picks from the truncated seismograms, and the arrows are the theoretical calculations. The model used is given in Figure 2.

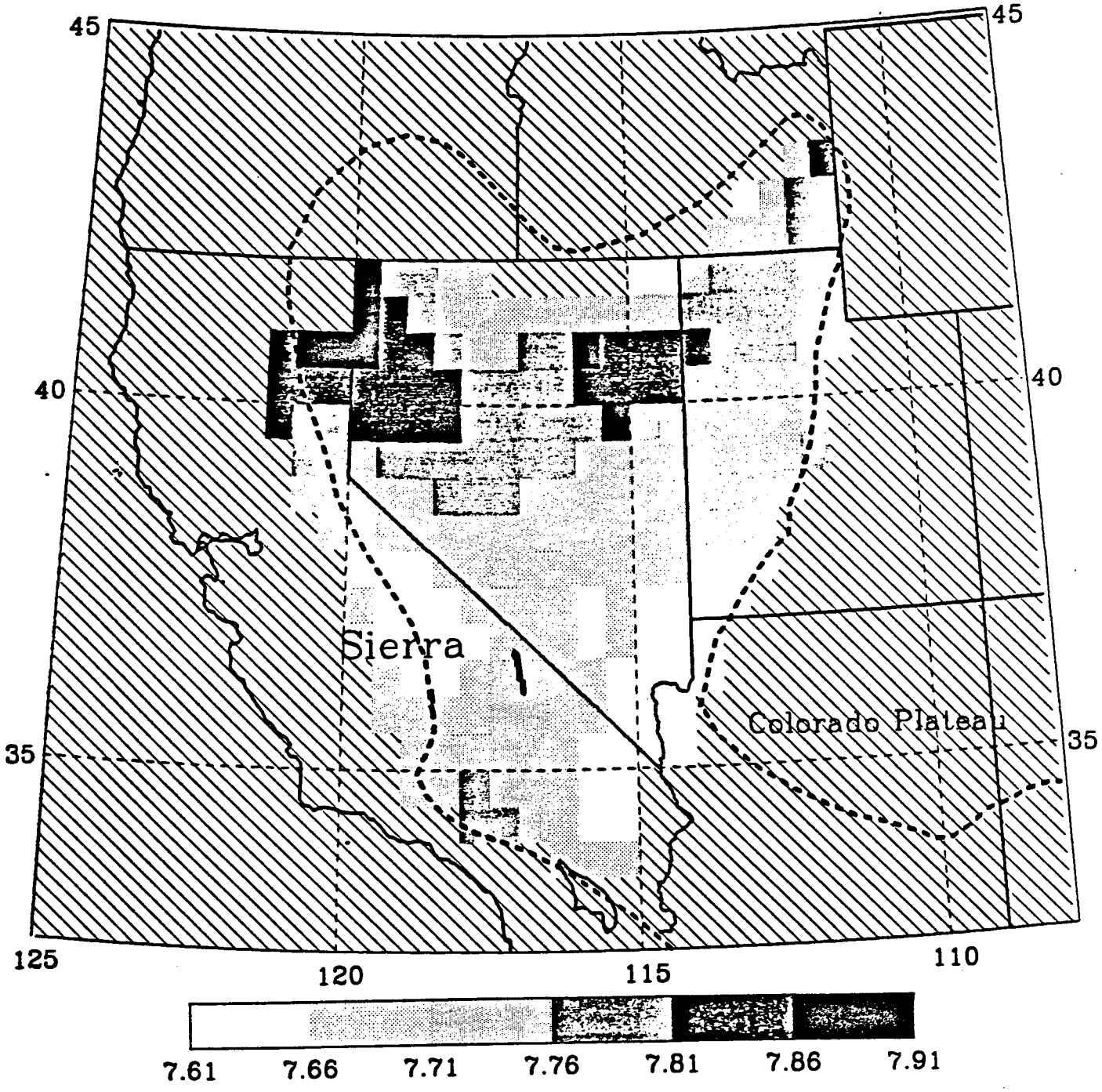

Figure 4. P_n velocity image for the Basin and Range province. Heavy dash lines depict the boundaries of the Basin and Range province. The diagonal ruled area are the area without enough resolution.

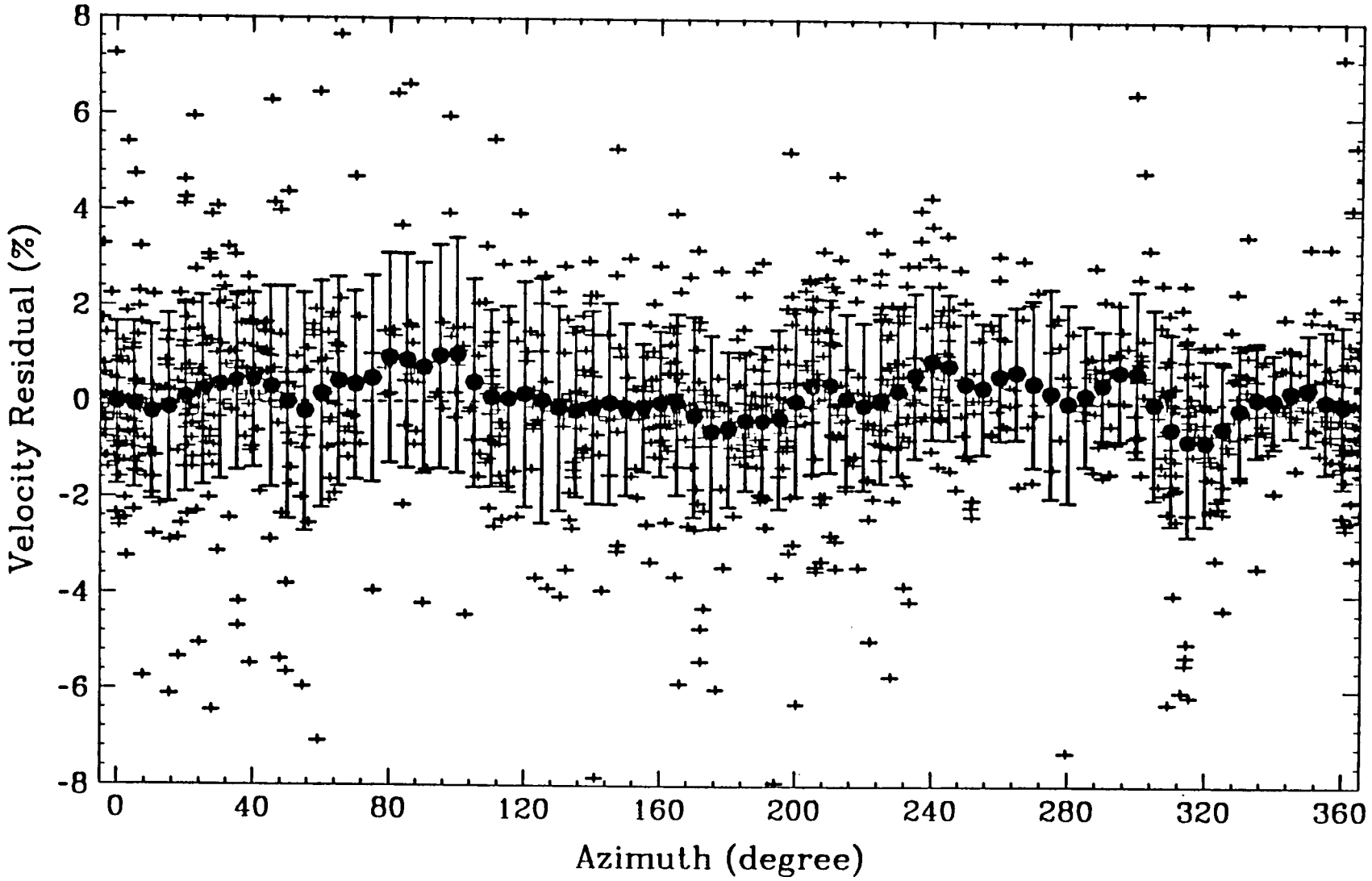

Figure 5. Velocity residuals ($\delta v/v$ in percent) calculated by using Equation (11), "+", and average velocity residuals (Equation (12)) in the 20 degree interval (solid dot) with error bars (square root of Equation (13)) , versus the azimuths of the paths.

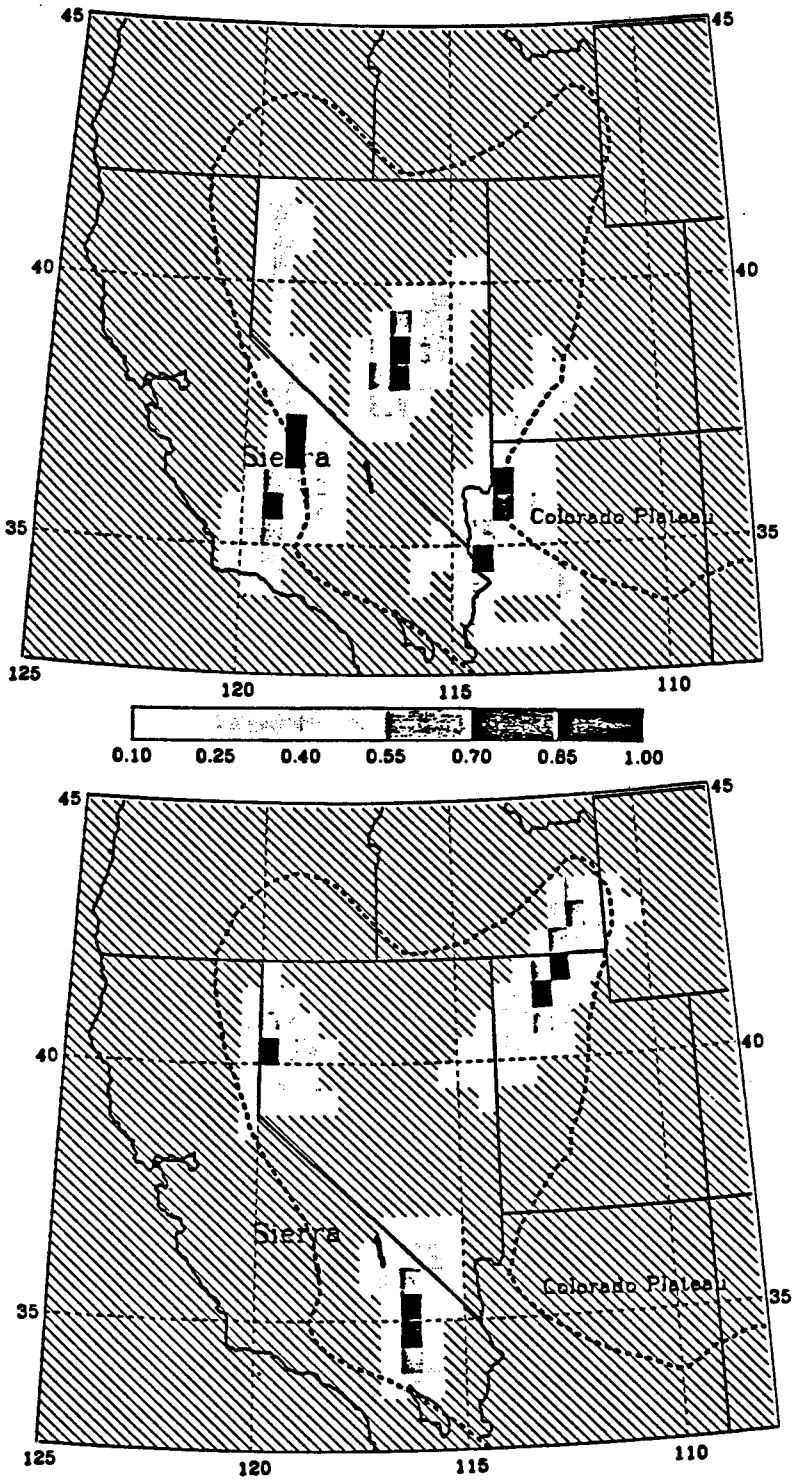

Figure 6. Point spread functions (p.s.f.) for six grids, five close to the boundaries, one in the center of the region. Without losing any information, I put three of them on one plot, since they do not overlap. p.s.f. of a) middle grid 2 degrees, left grid 5 degrees, and right grid 3 degrees; and b) left grid spreads 2 degrees, lower grid 2 degrees, and right grid 2.5 degrees. Heavy dash lines depict the boundaries of the Basin and Range province. The diagonal ruled area are the area without enough resolution, or with the amplitude less than 0.1.

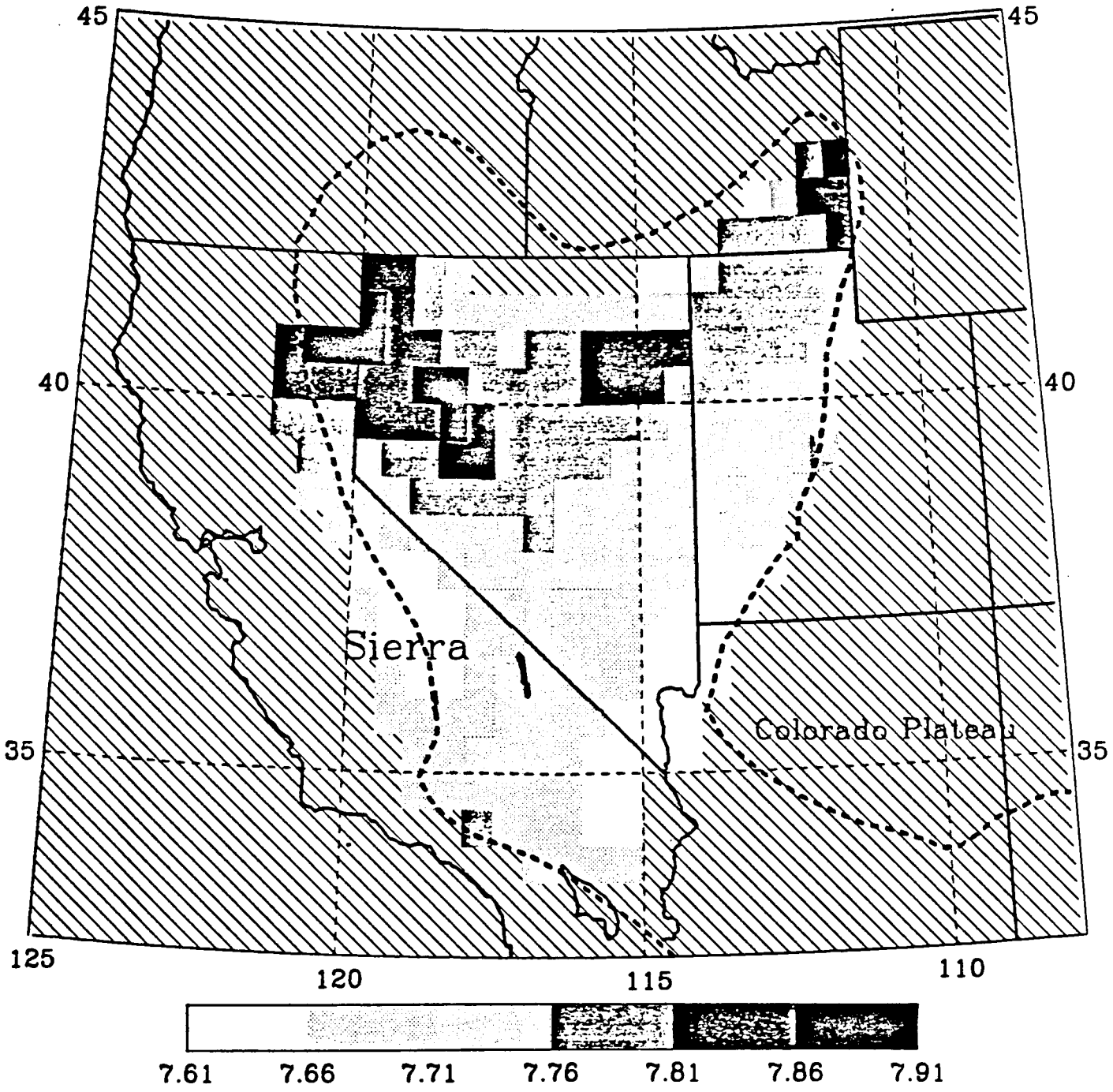

Figure 7. P_n velocity image for the Basin and Range province without correcting for mantle velocity gradient, i. e., assuming $\gamma' = 0.0$ seconds. The diagonal ruled area are the area without enough resolution.

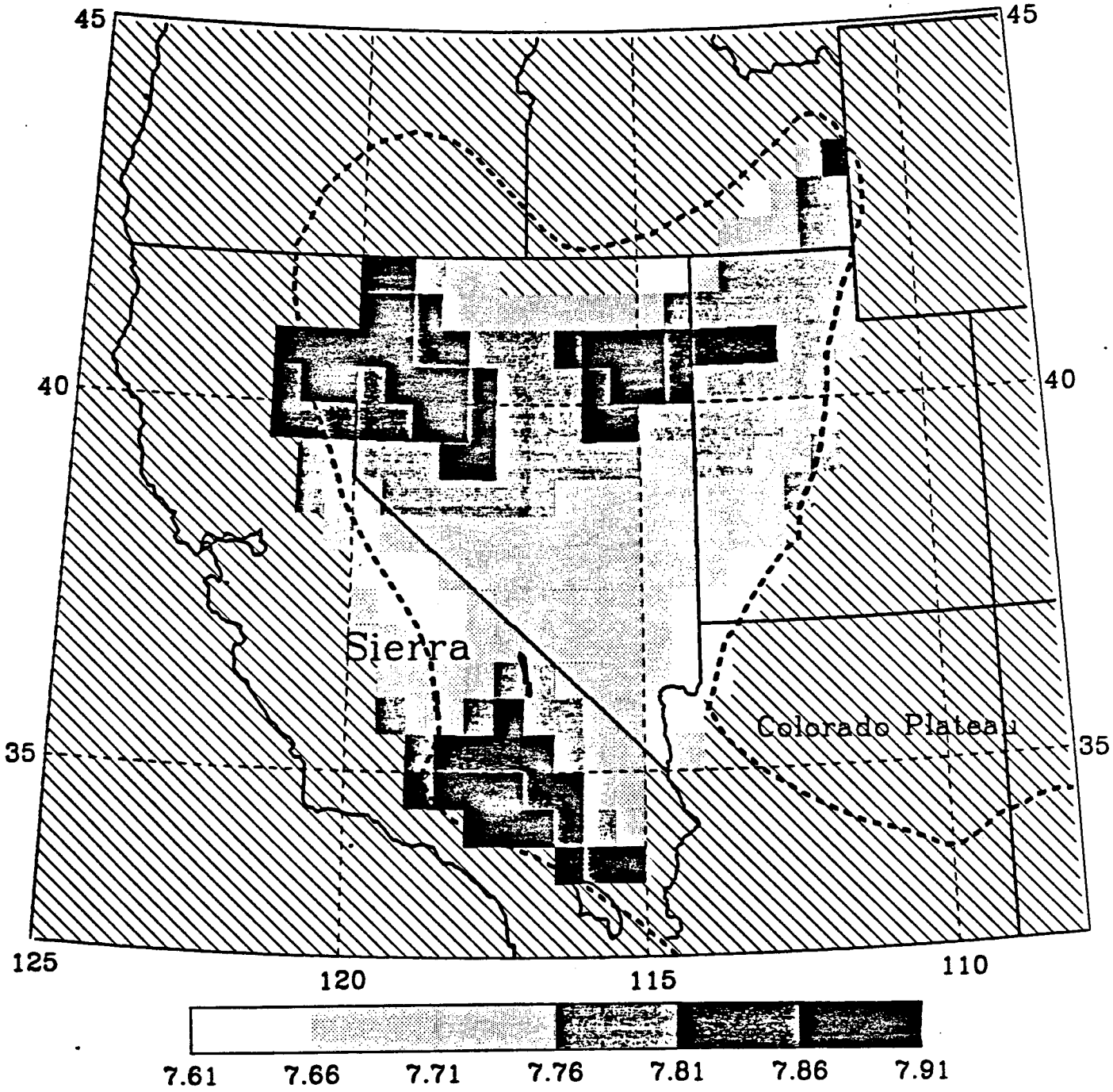

Figure 8. P_n velocity image for the Basin and Range province assuming a homogeneous crust and mantle.

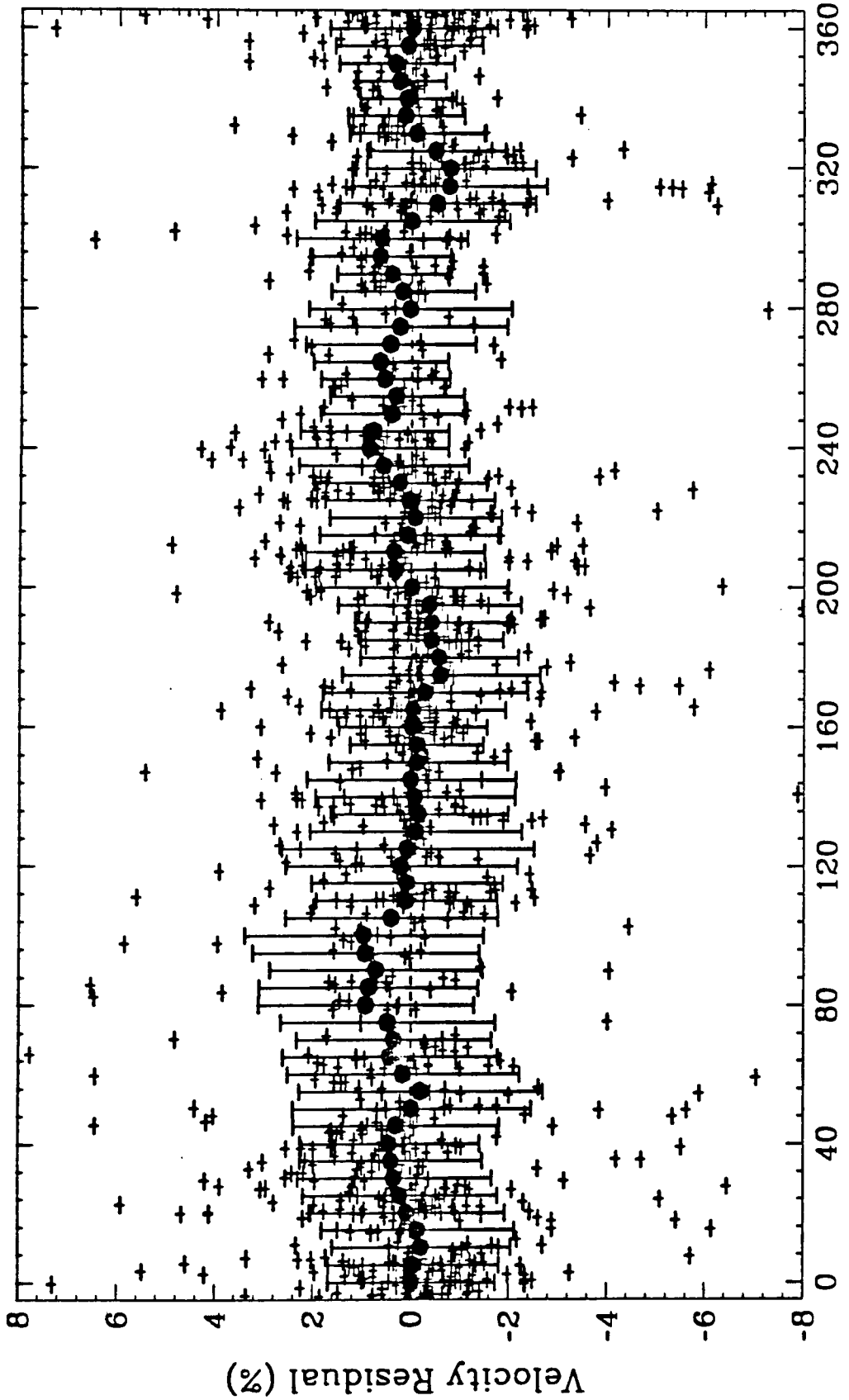

Figure 9. Velocity residuals, averaged velocity residuals after correcting the velocity distribution of Figure 7, versus the azimuths of the paths.

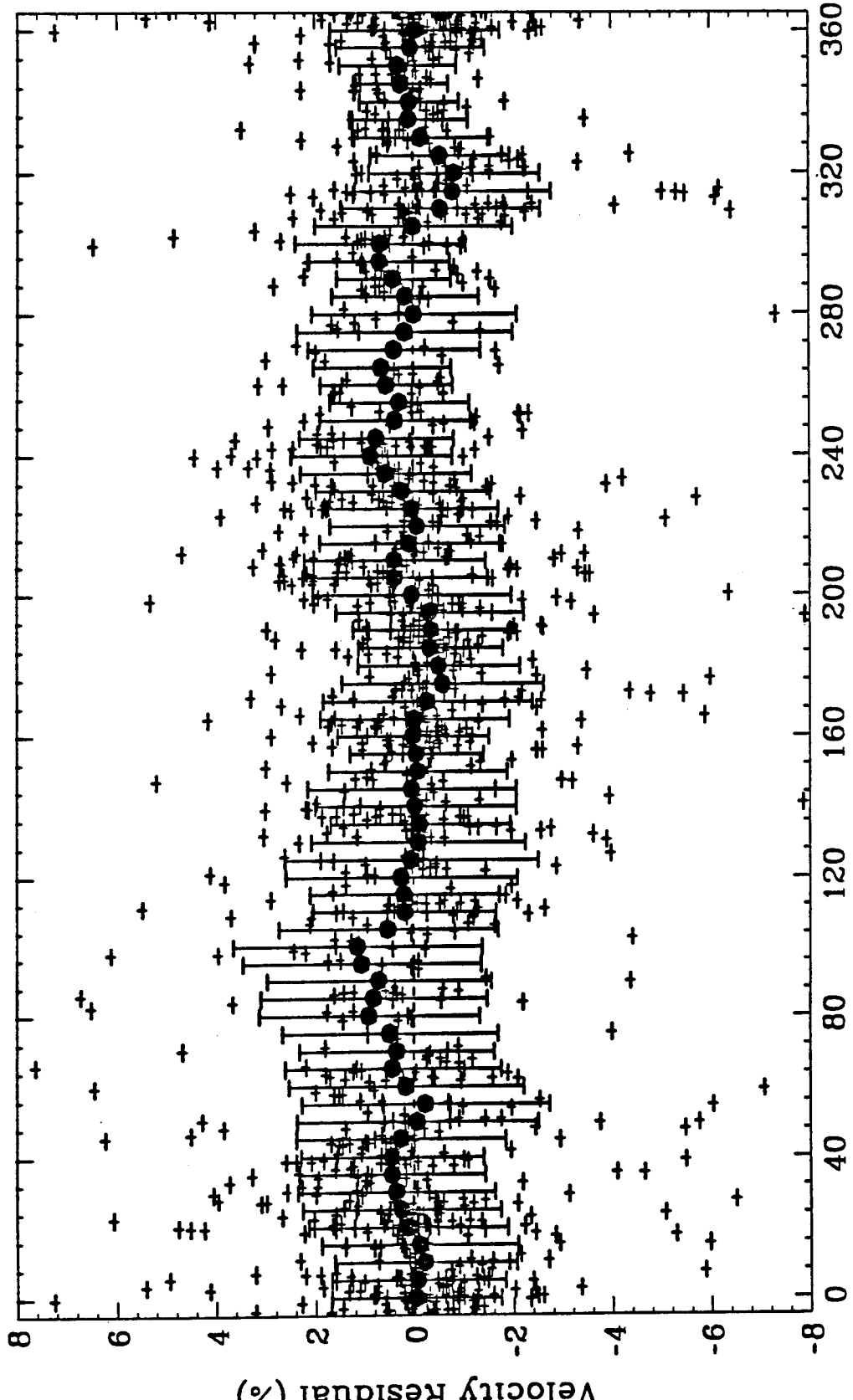

Figure 10. Velocity residuals, averaged velocity residuals after correcting the velocity distribution of Figure 8, versus the azimuths of the paths.

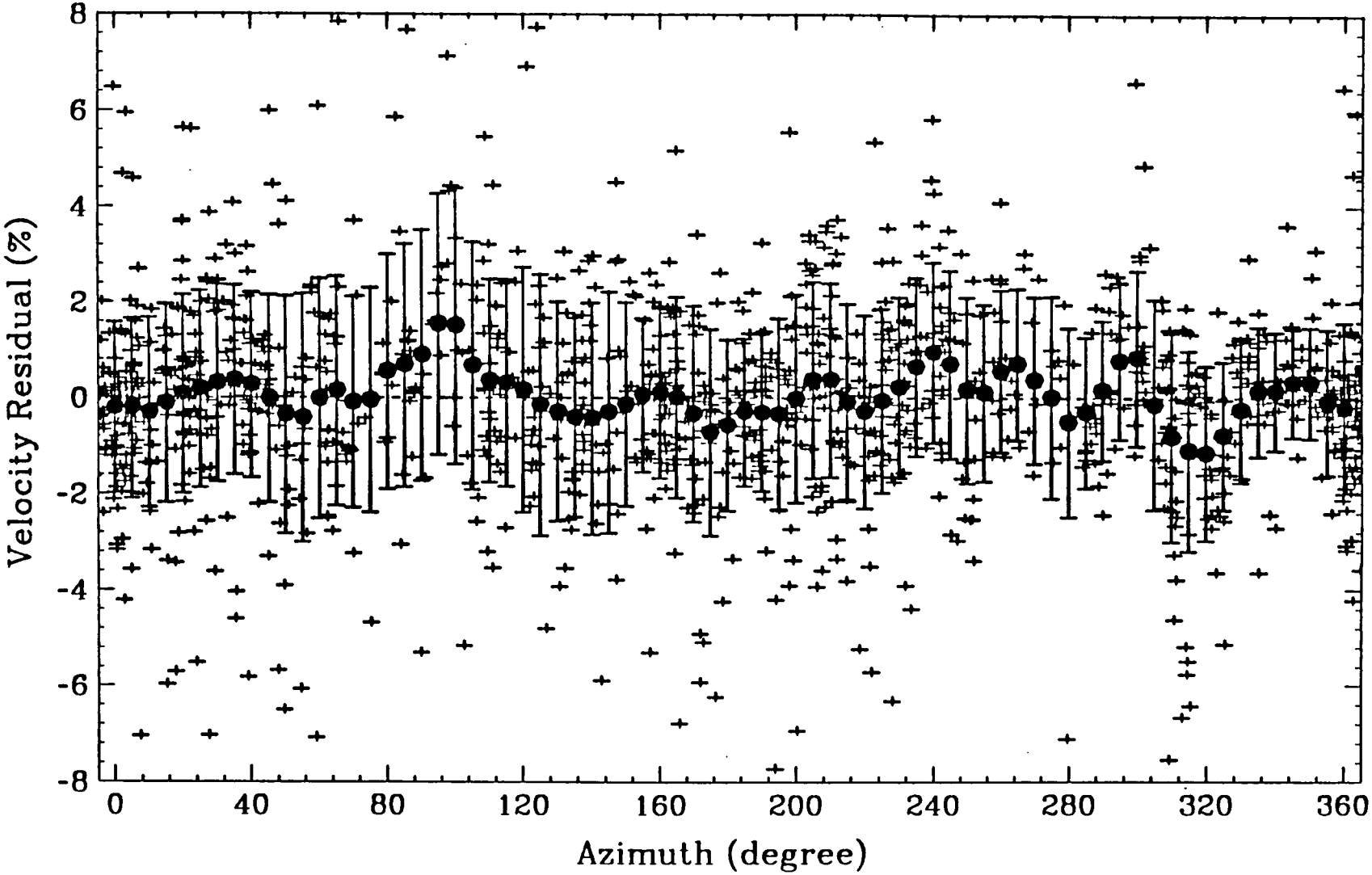

Figure 11. Velocity residuals, averaged velocity residuals before correcting the velocity distribution of Figure 8, versus the azimuths of the paths.

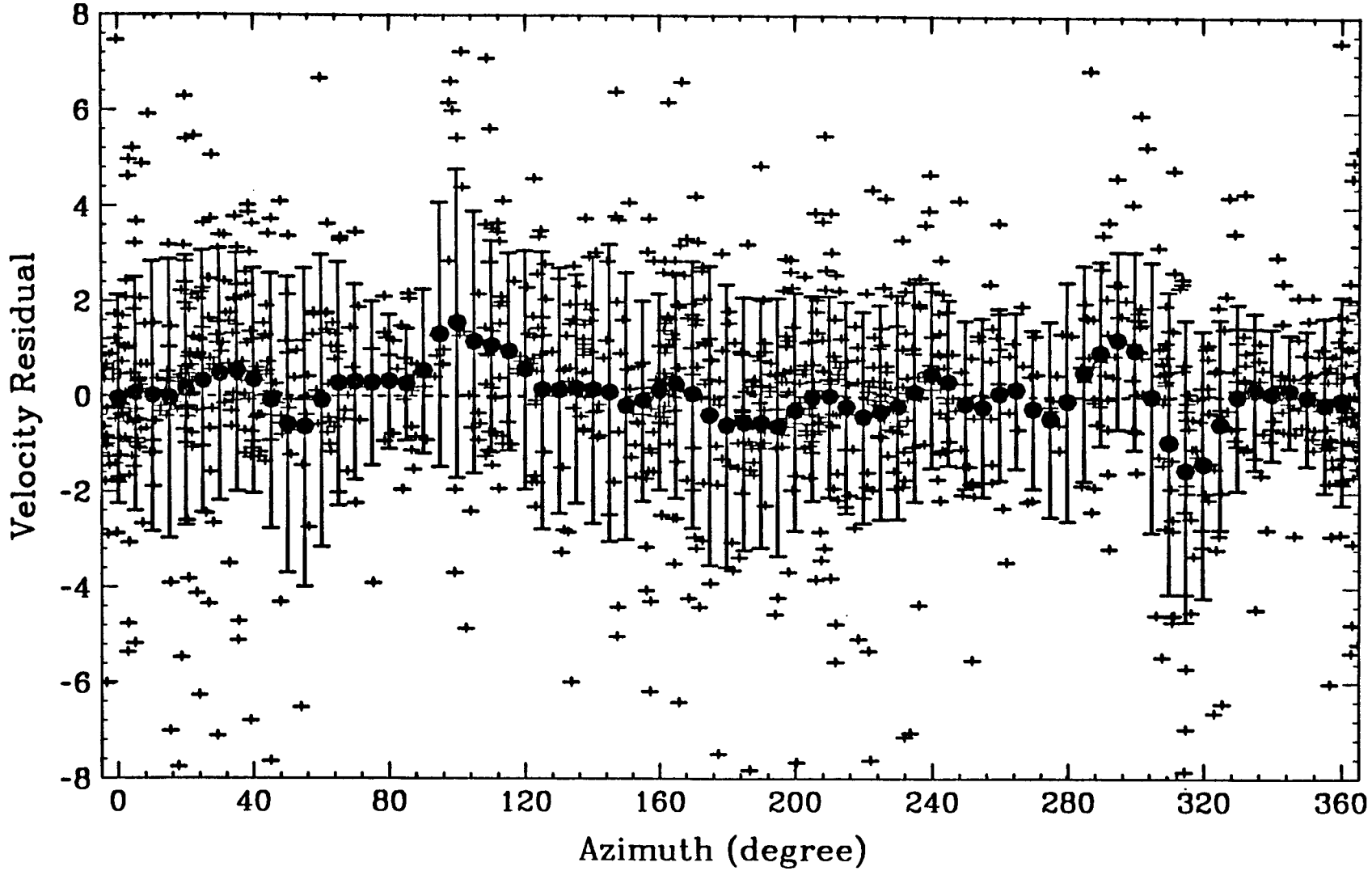

Figure 12. Velocity residuals, averaged velocity residuals versus the azimuths of the paths. The data used in this figure are the raw data after correcting the vertical travel times for the sources and receivers assuming a homogeneous crust and mantle, is the same as that produces the velocity image in Figure 8 and residuals in Figure 10, before the inversion and allocation procedure start.

Lateral Variation in Crustal Structure of the Northern Tibetan Plateau Inferred from Teleseismic Receiver Functions

by Lupei Zhu, Thomas J. Owens, and George E. Randall

Abstract A one-year period of passive-source recordings on the Tibetan Plateau includes more than 300 teleseismic events ranging from 35° to 95° in epicentral distance and with good back-azimuth coverage. This provides a chance to study the lateral variation of the crustal structure along the northern boundary of the plateau by investigating the variation of source-equalized P waveforms (receiver functions) with back-azimuth at stations BUDO, ERDO and TUNL located in this region. It is shown clearly that the waveforms of first 5 sec receiver functions vary with back-azimuth systematically: the radial components are symmetric across N-S axis while the tangential components are mirror-symmetric across this axis. All these can be modeled well by E-W striking dipping interfaces in the upper-middle crust. The strike direction is very consistent with the E-W trend of surface geology. Modeling a P-to-S converted phase in the radial components at each station shows that there is a mid-crust low velocity layer with its upper interface dipping 20-30° to the south. In addition, a shallow northwards-dipping interface under ERDO is responsible for the "double peaked" direct P arrivals in the radial components from certain back-azimuths and large tangential components. The low velocity layer, together with other geology and seismology observations, suggests that there is a hot, possible partial melting zone in the middle crust under the northern plateau. Alternately dipping velocity interfaces might be associated with some buried thrust faults in the brittle upper crust which accommodated crust shortening during some early stage of the plateau formation.

Introduction

The Tibetan Plateau, bounded by the Kunlun mountains in the north and Himalayas in the south, with its outstanding average elevation of 5 km and an exceptional area extent of nearly $7\times10^5 km^2$, has long been an interesting and challenging subject in geoscience. Although it is now generally agreed that the uplift of Tibet plateau is the result of the collision of Indian plate with Asia during Middle Eocene 45 million years ago, after the Tethys ocean lithosphere subducted completely beneath the Asia, the details of this collision mechanism and the plateau uplift still remain controversial. Several collision models have been proposed. Among the most influential ones are the underthrust model and its variants (Argand, 1924; Zhao and Morgan,

1985; Beghoul *et al.*, 1993), the crust shortening and thickening model (Dewey and Bird, 1970; Dewey and Burke, 1973), and the lateral crustal extrusion model (Molnar and Tapponnier, 1977; Tapponnier *et al.*, 1982). Due to lack of necessary constraints on the lithospheric structure under the plateau, it is difficult to discriminate among different models.

So far, most geological and geophysical investigations on the plateau were concentrated on the southern Tibet near the Himalayas. Comparatively, the structure near the northern boundary of the plateau was poorly resolved. Since the northern part of the plateau should play an equally important role as its southern counterpart during the forming of the plateau, better understanding of the crust and upper mantle structure under the northern plateau will help to constrain dynamic models of plateau formation.

Recently, as a joint research project between Institute of Geophysics, State Seismological Bureau, China, and University of South Carolina, State University of New York at Binghamton, 11 broadband 3-component seismic recorders were deployed on the plateau for one year of recording (Fig. 1). Three stations (TUNL, BUDO and ERDO) were placed across the northern boundary of the plateau, providing an ideal opportunity to study the crust and upper mantle structure in this area. In this paper, we will use teleseismic P waveform data to study the lateral variation of the crust structure. We will show that there is strong lateral variation in the crust of northern Tibet and that most of this variation is caused by E-W striking dipping velocity interfaces in the upper-middle crust.

Method

Teleseismic P waveform data contains information about both the source side and the receiver side structures. Using the method proposed by Langston (1979), the source and path effects can be removed from the P waveforms by deconvolving the vertical component from the horizontal components under the assumption that the vertical

component of the teleseismic recording consists primarily of the unwanted source and path effects. The source-equalized teleseismic waveform which is called the receiver function is most sensitive to the P-to-S conversions from structures beneath the recording site (Owens *et al.*, 1984).

The radial component of broadband receiver functions is often modeled by horizontally stratified velocity structure using a time-domain inversion technique (Owens *et al.*, 1984; Ammon *et al.*, 1990). This method has been applied to numerous areas and proven to be efficient in obtaining the velocity-depth variation of the crust and the Moho depth. However, if the tangential component of receiver function is comparable in amplitude to the radial component, which generally indicates that there is strong lateral heterogeneity within the crust beneath the site, modeling the details of the radial component with horizontally stratified velocity will lead to erroneous results.

One of the special cases of lateral heterogeneity is the dipping planar velocity interface in the crust. In this case, both the radial and tangential component vary with back-azimuth in a quite predictable pattern. Figure 2 shows the variation of synthetic receiver functions for a crust model which contains a mid-crustal low velocity layer with its upper interface dipping 20° to the south. The interface is at depth of 20 km where the S velocity jumps from 3.0 km/sec below it to 3.5 km/sec above. The Moho is at a depth of 65 km. Teleseismic ray parameter is 0.068 sec/km which corresponds epicentral distance of 50°. Synthetics are calculated by using a 3D ray-tracing method of Langston (1977). It can be seen that the waveform variation with back-azimuth is very systematic: the radial components are symmetric across a line parallel to the dip direction of the interface, while the tangential components are mirror-symmetric about this direction (indicated by arrow in the figure). Tangential component has the largest energy in the strike direction and will be zero when ray comes from direction parallel to the dip direction. The P-to-S converted wave generated at the dipping interface is labeled as phase A. This negative-amplitude phase emerges in the southern back-

azimuths with maximum amplitude from the dip direction and vanishes gradually away from the dip direction.

So, if the dipping interface is the major cause of lateral heterogeneity under the station, it is very easy to determine the dip and strike direction by looking at the back-azimuthal profile of the receiver functions. The dip angle, velocity contrast, and the depth of the interface can be obtained by modeling the amplitude and arrival time of the converted phase from the interface, although a trade-off exists between the dip angle and the velocity jump across the interface (Owens *et al.*, 1988). Figure 3a shows the variation of absolute amplitude of the P-to-S converted phases from above dipping interface with different dip angles. Figure 3b is the variation of maximum amplitude with velocity contrast at the interface. It can be seen that the dip angle controls the shape of the amplitude variation with back azimuth, while the velocity difference across the interface contributes mainly to the maximum amplitude (Fig. 3). The dip angle also affects the maximum amplitude. But to produce same maximum amplitude with velocity contrast differing 0.1 km/sec, the dip angles will differ more than 10° (Fig. 3b), which will have quite different shapes of amplitude variation with back-azimuth (Fig. 3a). For this reason, if data set has enough back-azimuth sampling, reasonable constraints can be made on the dip angle and velocity contrast of the interface.

Data

Ten of the 11 stations in the experiment were equipped with Streckeisen STS-2 sensors. Station TUNL was equipped with Guralp CMG-3ESP sensor. The STS-2 has a broad velocity response with corner frequencies of 0.0083 Hz and 50 Hz and the CMG-3ESP has corner frequencies of 0.033 Hz and 30 Hz. 40 samples/sec sampling rate was used for recording waveforms of regional and teleseismic events. Details about the instrumentation of the experiment can be found in Owens *et al.*, 1993.

More than 300 teleseismic events ranging between 35° to 95° in epicentral distance were recorded during the Tibetan experiment. A preliminary study of the receiver functions of teleseismic events from certain back-azimuths on 3 stations (TUNL, WNDO and XIGA) located in the northern, central and southern plateau has shown the great thickness of crust (60 to 80 km) and the difference of velocity structures between north-central and southern Tibet (Zhu *et al.*, 1992). Large tangential components were also observed in TUNL and XIGA.

Three stations, TUNL, BUDO, and ERDO, were located near the north boundary of the plateau which is defined by an E-W striking fault system, the Kunlun Mountain Fault System (Fig. 1). The elevation increases from 3 km in the Qaidam Basin to more than 4.5 km inside the plateau. The surface geology in this region includes highly deformed Permian subduction-related rocks and Upper Paleozoic pluton rocks (Dewey *et al.*, 1988). The Kunlun fault system consists of several large left-lateral strike-slip faults. Some thrust faults were discovered during several recent geotraverses, for example, the South Qaidam Border Thrust Fault and Fenghuoshan thrust faults (Molnar *et al.*, 1987; Kidd *et al.*, 1988).

Figure 4 is the distribution of teleseismic events used in this study. The good back-azimuthal coverage of teleseismic events enables us to study the lateral variation of the crustal structure in the area from the variation of the receiver function waveforms with back-azimuth at each of these stations. The 3-component teleseismic recordings were cut with a time window of 180 sec length beginning 60 sec before P arrival. Then horizontal components were rotated to radial and tangential directions and deconvolved with vertical component in frequency domain. Gaussian parameter of 2.5 was used to exclude frequencies above 1 Hz. To make the deconvolution algorithm stable, we used a range of water-levels from 0.1 to 0.0001 and chosed the best one from them. Details on the calculation of receiver function are described in some published papers (Owens *et al.* 1984; Ammon *et al*, 1990).

For each station, the teleseismic events are divided into groups of back-azimuth range less than 10°, according to their natural distribution with respect to that station and the waveform similarity of the receiver functions. We found that the difference in epicentral distance does not affect the waveforms much, so some of the groups span a distance range of about 20°. The receiver functions in each group are then stacked. The back-azimuthal/distant range and the number of events for each stacking suite are listed in Table 1.

Figure 5 is the back-azimuthal profiles of the stacked receiver functions. It is clear that there is strong lateral variation in the upper-middle crustal structure of this region as evidenced by the large tangential components in the first 5 sec on all these 3 stations. Also the waveforms vary with back-azimuth in the pattern predicated by dipping interfaces we described above. Both the symmetry of radial components and the mirror-symmetry of tangential components across N-S direction are obvious in the first 5 sec of the receiver functions. The tangentials are nearly zero in the N-S direction (as indicated by arrows in Figure 5). Largest tangential components are on events arriving from the east and west directions (back azimuths of about 90-100° and 270-280°) with opposite polarities.

Modeling Results

One prominent feature observed in the radial receiver functions is a mid-crust P-to-S converted phase in back-azimuth range of about 100° to 300° (indicated by dashed-lines in Figure 5). This negative polarity arrival is well illustrated at BUDO (time delay 3.2 sec with respect to direct P arrival) and also can be identified at TUNL (2.4 sec) and ERDO (3.8 sec). Since there is no large converted phase before it, this phase could not be multiple converted phase. So its negative polarity indicates that it is generated at top of a lower velocity layer (as shown in synthetic receiver functions in

Fig. 2). The variation of the amplitude of this phase with back-azimuth is caused by the southward dipping of the interface.

We measure the absolute amplitudes of this phase at the radial components from different back-azimuths and fit them with synthetical calculations by trial-and-error forward modeling. A range of S-velocity contrasts from 3.4/3.1 to 3.6/2.8 across the interface and dip angles from 10° to 30° have been tested. We use maximum amplitude to determine the velocity contrast and dip direction and use the shape of the amplitude variation with back-azimuth to determine the dip angle. Figure 6 gives the modeling results. There is very good back-azimuth sampling at BUDO which leads to substantial constraint on the velocity contrast (3.6/2.9) and dip angle (25°) (Fig. 6b). Station TUNL and ERDO do not have enough data points to resolve the dip angles. The velocity contrast is 3.5/3.0 across the interface and the dip angle can be 25±5° (at TUNL) or 20±5° (at ERDO). The depth of the mid-crustal dipping interface at each station is determined by the arrival time of the converted phase, assuming the average upper crust S-velocity of 3.5 km/sec. The results are 15 km for TUNL; 24 km for BUDO and 30 km for ERDO.

Another feature of radial receiver functions is the apparent time shift of direct P arrivals from back-azimuths 30° and 315° at ERDO (indicated by blacken dots in Fig. 5c). It is actually produced by a shallow dipping interface which causes the direct P arrival very small and the Ps-wave generated on the interface appears to be the first arrival. Such shallow dipping interface effect on the receiver function has been modeled and discussed by Owens and Crosson (1988). We found, by adjusting the depth, dip angle and velocity contrast of the interface, that a low velocity top layer (S-velocity 2.5 km/sec) of thickness 4 km with bottom interface dipping 15° to the north can model both the radial and tangential waveform of first 2-3 sec very well (Fig. 7)

Conclusions and Discussion

In summary, the waveform variation of receiver functions with back-azimuth at three stations located in the northern Tibetan Plateau shows that there are strong lateral heterogeneities within the upper-middle crust in this region. The waveform variation pattern also indicates that it is mainly produced by E-W striking dipping interfaces. The strike direction is very consistent with the E-W trend of surface geology. Modeling a negative-polarity P-to-S converted phase in the radial component at each station shows that there is a mid-crust low velocity layer with upper interface dipping 20-30° to the south. In addition, a shallow northwards-dipping interface under ERDO is responsible for the "double peaked" direct P arrivals in the radial components from certain back-azimuths and large tangential components.

Our result of mid-crust low velocity layer (LVL) is consistent with previous results from phase velocity dispersions of surface wave (Romanowicz, 1982; Brandon and Romanowicz, 1986). The modeling shows that the shear velocity in the middle crust could by as low as 2.9 km/s. Due to difficulty of identifying converted phase from bottom of the LVL, we are unable to determine the thickness of the LVL. But the LVL itself has important indication on the crustal structure of the plateau. One of possibilities to get such low shear velocity at depth larger than 20 km is partial melting. Partial melting is effective in decreasing velocities under high presure (Anderson, 1989). The very lower average S-velocity (less than 3.5 km/s) from surface wave dispersion data led Chen and Molnar to suggest that lower crust of the northern plateau is in partial melting (Chen and Molnar, 1981). Recent earthquake relocations on Tibet plateau show that most earthquakes occur only in the depth range between 5 and 15 km (Chen and Molnar, 1983; Zhao and Helmberger, 1991). The partial melting is also supported by the observation of Quaternary volcanic activities in the northern Tibet (Deng, 1978; Pearce and Mei, 1988). The high temperature in the crust could be due

to the concentration of crust material during the crust-shortening or high heat flow from the upper mantle.

The E-W striking dipping interfaces of our modeling results might be associated with some buried thrust faults in the brittle upper crust in this northern margin of the plateau. For example, the shallow northwards-dipping interface under ERDO could be related to the Fenghuoshan thrust faults which run EW in the south of the station. It is estimated that large amount of crust shortening has occurred during the formation of the plateau. Palaeomagnetic data provided a rough relative movement between the India plate and the 'stable' Eurasia. It shows that only small fraction of India crust (400 km) was absorbed since the collision and most of this fraction can be found accumulated on the Himalayan front instead of underthrusting into the Tibet crust (Dewey *et al.*, 1988). On the other hand, about 2000 km crust shortening has occurred between the Indo-Zanbo collision suture and the Siberia (Patriat and Achache, 1984; Lin, 1988). Accommodating such large amount of crust shortening needs thrust faults within the plateau or along the north and south boundaries. Large scale thrust faults exist along the Himalayan front and north-west boundary between Tibet and Tarim Basin. Recent geological expeditions also found evidence of thrust faults in northern Tibet (Molnar *et al.*, 1987; Tapponnier *et al.*, 1990).

Shallow and mid-crust dipping interfaces have noticeable impact on the modeling of deep structure such as the Moho. As demonstrated in our synthetic receiver functions in Figure 2, the multiple converted phases of the dipping interface will interfere with the Moho Ps and make the amplitude of Moho Ps varying with back azimuth. This effect is also seen in the observed receiver functions. For crust structure of Tibet with thickness of about 65 km, the predicted arrival time of Moho Ps is 7.5-8s after the direct P. However, at all three stations, we have not observed "stable" Moho Ps on the receiver functions profiles (Fig. 5). ERDO's receiver functions are almost dominated by the converted waves from shallow structure so that it is difficult to identify

the Moho Ps.

We found that the receiver function is an efficient way to study the lateral variation of crustal structure, provided there are substantial teleseismic events with good back-azimuth distribution have been recorded. Modeling both the radial and tangential receiver function requires ray-tracing in 3D medium. Although we have modeled successfully the variation pattern of radial receiver function with dipping planar interface, the large tangential component amplitudes remain hard to match. More sophisticated techniques such as finite difference method might be needed.

Acknowledgments

This work was supported at University of South Carolina under NSF grants EAR-9196115. It has also been supported at Caltech by the Department of Defense as monitored by the Air Force Office of Scientific Research under contract F49620-92-J-0470.

References

Ammon, C. J., G. E. Randall, and G. Zandt (1990). On the nonuniqueness of receiver function inversions, *J. Geophys. Res.* **95**, 15,303-15,318.

Anderson, D. L. (1989). *Theory of the earth* Blackwell Scientific Publications, Boston, 51-54.

Argand, E. (1924). La tectonique de l'Asie, *Proc. 13th Int. Geol. Congr., Brussels 1924* **7**, 171-372.

Beghoul, N., M. Barazangi, and B. Isacks (1993). Lithospheric structure of Tibet and western North America, mechanisms of uplift and a comparative study, *J. Geophys. Res.* **98**, 1997-2016.

Brandon C. and B. Romanowicz (1986). A no-lid zone in the central Chang-Thang platform of Tibet, evidence from pure path phase-velocity measurements of long period Rayleigh-waves, *J. Geophys. Res.* **91**, 6547-6564.

Deng, W. A. (1978). A preliminary study on the petrology and petrochemistry of Quaternary volcanic rocks of northern Tibet autonomous region, *Acta Geol. Sinica* **52**, 148-162.

Dewey, J. F. and J. M. Bird (1970). Mountain belts and the new global tectonics, *J. Geophys. Res.* **75**, 2625-2647.

Dewey, J. F. and K. Burke (1973). Tibetan, Variscan and Precambrian basement reactivation: products of a continental collision, *J. Geol.* **81**, 683-692.

Dewey, J. F., R. M. Shackleton, C. Chang, and Y. Sun (1988). The tectonic evolution of the Tibetan Plateau, *Phil. Trans. R. Soc. Lond.* **A327**, 379-413.

Kidd W. S. F., Y. Pan, C. Chang, M. P. Coward, J. F. Dewey, A. Gansser, P. Molnar, R. M. Shackleton, and Y. Sun (1988). Geological mapping of the 1985 Chinese-British Tibetan (Xizang-Qinghai) Plateau Geotraverse rout, *Phil. Trans. R. Soc. Lond.* **A327**, 287-305.

Langston, C. A. (1977). The effect of planar dipping structure on source and receiver responses for constant ray parameter, *Bull. Seism. Soc. Am.* **67**, 1029-1050.

Langston, C. A. (1979). Structure under Mount Rainier, Washington, inferred from teleseismic Body waves, *J. Geophys. Res.* **84**, 4749-4762.

Lin, J. and D. Watts (1988). Palaeomagnetic results from the Tibetan plateau, *Phil. Tran. R. Soc. Lond.* **327**, 239-262.

Molnar, P. and P. Tapponnier (1977). Relation of eastern China to the India-Eurasia collision: application of slip-line field theory to large-scale continental tectonics, *Geology* **5**, 212-216.

Molnar P. and W. Chen, 1983, Focal depths and fault plane solution of earthquakes under the Tibetan Plateau, *J. Geophys. Res.* **88**, 1180-1196.

Molnar, P., B. C. Burchfiel, K. Liang, and Z. Zhao (1987). Geomorphic evidence for active faulting in the Altyn Tagh and northern Tibet and qualitative estimates of its contribution to the convergence of India and Eurasia, *Geology* **15**, 249-253. *J. Geophys. Res.* **72**, 665-689.

Owens, T. J., G. Zandt, and S. R. Taylor (1984). Seismic evidence for ancient rift beneath the Cumberland plateau, Tennessee: A detailed analysis of broadband teleseismic P waveforms, *J. Geophys. Res.* **89**, 7783-7795.

Owens, T. J. and R. S. Crosson (1988). Shallow structure effects on broadband teleseismic P waveforms, *Bull. Seism. Soc. Am.* **77**, 96-108.

Owens, T. J., G. E. Randall, F. T. Wu, and R. S. Zeng (1993). PASSCAL instrument performance during the Tibetan plateau passive seismic experiment, *Bull. Seism. Soc. Am.* **83**, 1959-1970.

Patriat, P. and J. Achache (1984). India Eurasia collision chronology has implications for crustal shortening and driving mechanism of plates, *Nature* **311**, 615-621.

Pearce, J. A. and H. Mei (1988). Volcanic rocks of the 1985 Tibet Geotraverse: Lhasa to Golmud, *Phil. Tran. R. Soc. Long.* **327**, 169-201.

Romanowicz, B. (1982). Constraints on the structure of the Tibet Plateau from pure path phase velocities of love and Rayleigh-waves, *J. Geophys. Res.* **87**, 6865-6883.

Tapponnier, P., G. Peltzer, A. Y. Ledain, R. Armijo, and P. Cobbold (1982). Propagating extrusion tectonics in Asia: new insight from simple experiments with plasticine, *Geology* **10**, 611-616.

Tapponnier, P., B. Meyer, J. P. Avouac, G. Peltzer, and Y. Gaudemer (1990). Active thrusting and folding in the Qilian-Shan, and decoupling between upper crust and mantle in northeastern Tibet, *Earth Planet. Sci. Lett.* **97**, 382-403.

Zhao, W and J. Morgan (1985). Uplift of the Tibet Plateau, *Techtonics* **4**, 359-369.

Zhao, L. and D. V. Helmberger, 1991, Geophysical implication from relocation of Tibetan earthquakes - hot lithosphere, *Geophys. Res. Lett.* **18**, 2205-2208.

Zhu, L., R. Zeng, F. Wu, T. J. Owens, and G. E. Randall (1993). Preliminary study of crust-upper mantle structure of the Tibet Plateau by using broadband teleseismic body waveforms, *Acta Seism. Sinica* **6**, 305-316.

Seismological Laboratory
California Institute of Technology
Pasadena, California 91125
(L.Z.)

Department of Geological Sciences
University of South Carolina
Columbia, South Carolina 29208
(T.J.O. and G.E.R.)

Table 1
Back Azimuthal/Distant Ranges and Number of Events of Stacking Suites

TUNL			BUDO			ERDO		
Baz°	Δ°	number	Baz°	Δ°	number	Baz°	Δ°	number
6± 1	45± 1	2	5± 0	46± 0	1			
27± 1	89± 5	7	27± 1	90± 5	5	26± 1	92± 5	4
45± 3	54± 7	10	43± 4	56± 8	11	41± 5	59±10	10
58± 4	40± 4	36	59± 6	41± 4	33	57± 5	42± 4	20
68± 4	36± 1	11						
78± 3	36± 2	14	79± 5	38± 2	19	75± 6	39± 2	9
88± 5	40± 3	21	89± 2	42± 3	7	89± 4	44± 4	5
102± 5	48± 1	5	101± 4	49± 1	4			
			110± 1	84± 3	9			
115± 4	62±12	14	115± 4	68± 7	18	112± 4	71±10	13
127± 5	46± 8	20	130± 6	47± 7	31	128± 6	48± 8	27
138± 5	47± 6	23	145± 3	50± 2	3	143± 3	50± 2	3
153± 4	48± 1	4						
166± 1	41± 1	5	161± 5	43± 3	5	164± 0	39± 0	1
182± 0	52± 0	2	181± 0	51± 0	2	180± 0	50± 0	2
212± 0	59± 0	1	211± 0	58± 0	1	210± 0	57± 0	1
			243± 0	40± 0	1			
255± 0	59± 7	2	255± 0	51± 0	1			
266± 0	32± 0	2						
272± 1	37± 0	2	270± 4	33± 2	3	272± 3	33± 1	2
			285± 0	37± 2	2			
290± 4	46± 7	6	291± 1	47± 5	4	289± 3	38± 4	4
303± 0	54± 0	1	303± 0	53± 0	1	303± 0	53± 0	1
346± 0	54± 0	1	346± 0	55± 0	1			
Total		205			161			102

Figure Captions

Figure 1. Tectonic sketch map of Tibet Plateau (modified from Dewey *et al.*, 1988). Grayed areas are below 3 km elevation.

Figure 2. Synthetic receiver function variation with back-azimuth for a model containing a mid-crust low velocity layer with its upper interface dipping 20° to the south (see the paper). P-to-S converted phase from the dipping interface is indicated by dashed line.

Figure 3. (a) Amplitude variation with back-azimuth of P-to-S converted phase from dipping interfaces at different dip angles, (b) maximum amplitude variation with velocity contract across the dipping interface at different dip angles. The S-wave velocity differences are from 0.3 to 0.8 km/s correspond to S-wave velocity contrasts of 3.4/3.1, 3.5/3.1, 3.5/3.0, 3.6/3.0, 3.6/2.9, and 3.6/2.8 across the interface. Teleseismic ray parameter is 0.068 s/km.

Figure 4. Teleseismic events used in this receiver function study, their epicentral distances range from 35° to 95° with respect to station BUDO. The area in figure 1 is shown as gray box in the figure.

Figure 5. Variation of receiver functions with back-azimuth in station (a) TUNL, (b) BUDO, and (c) ERDO. Arrows point to the back-azimuth with minimum tangential energy. Also indicated by blackened dots are mid-crust P-to-S converted phases.

Figure 6. Measured absolute amplitudes of the mid-crust converted phases at three stations. Dashed error bar means only one event is available in this stacking suite so average standard deviation of other stacking suites is used. Solid line are synthetic calculations with the velocity contrast and dip angle shown in the figure.

Figure 7. Synthetic receiver functions showing the effect of shallow dipping interface under ERDO. Dashed line indicats the Ps phase from the dipping interface (see paper).

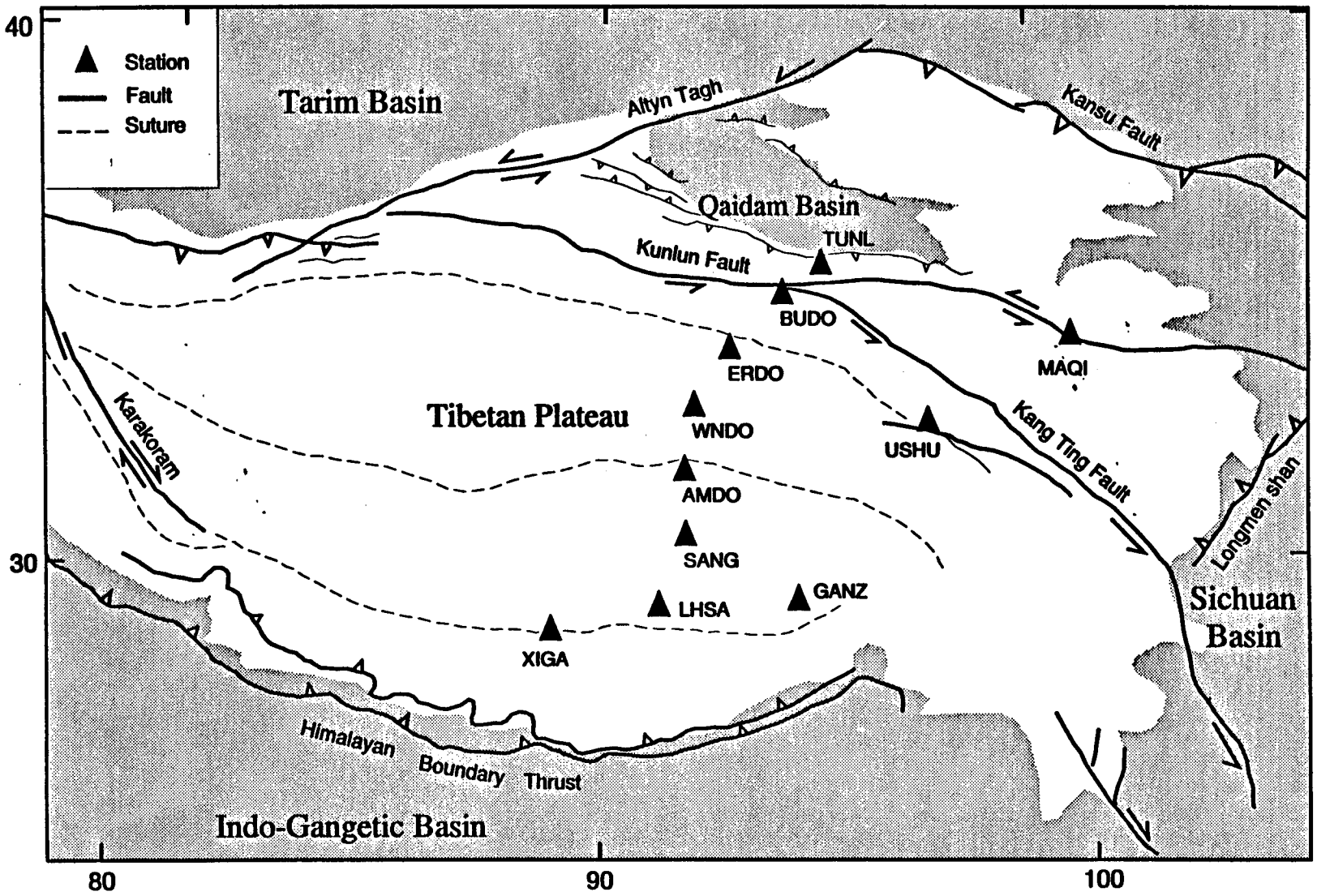

Figure 1. Tectonic sketch map of Tibet Plateau (modified from Dewey *et al.*, 1988). Grayed areas are below 3 km elevation.

Fig 1

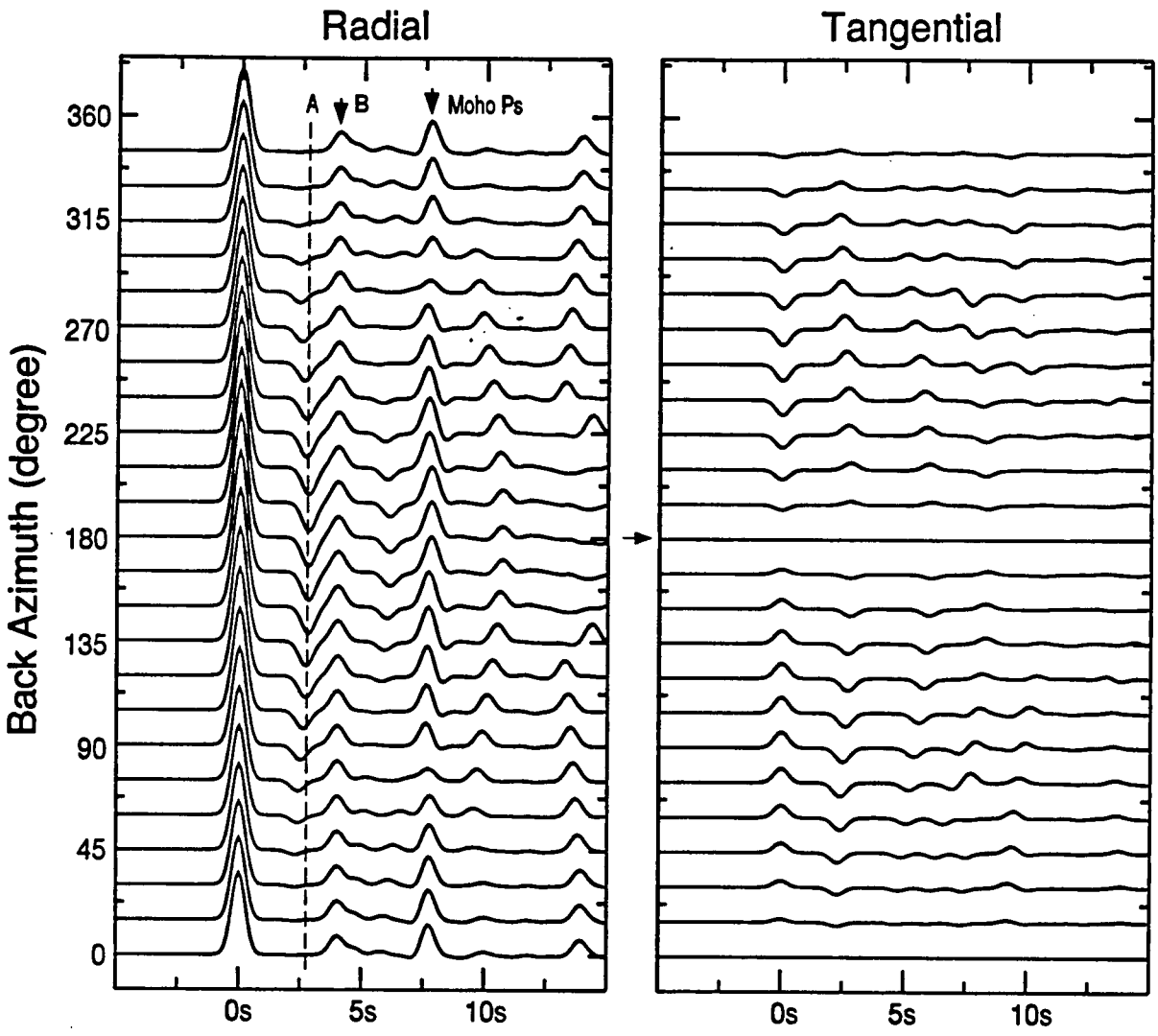

Figure 2. Synthetic receiver function variation with back-azimuth for a model containing a mid-crust low velocity layer with its upper interface dipping 20° to the south (see the paper). P-to-S converted phase from the dipping interface is indicated by dashed line.

Fig 2

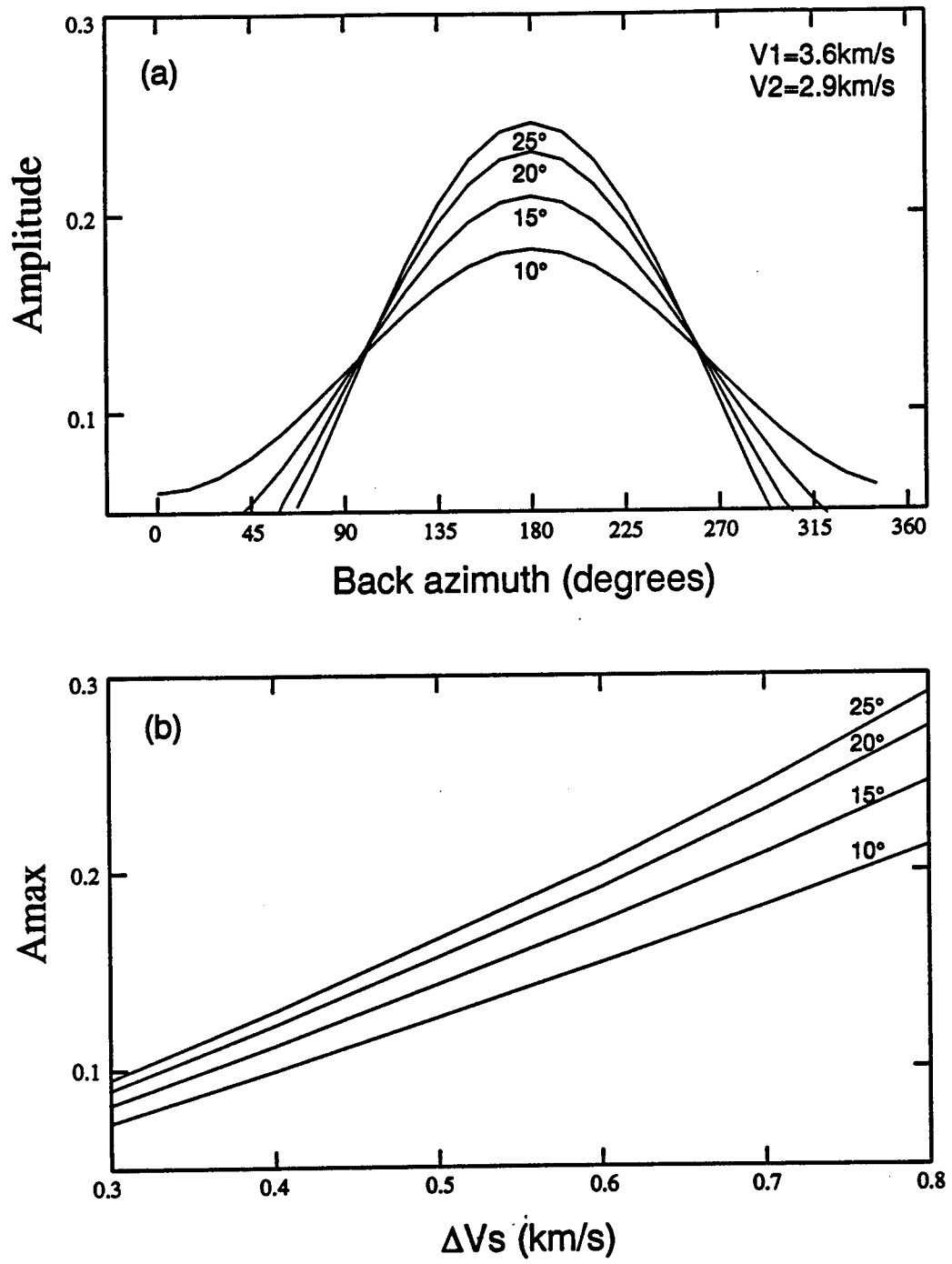

Figure 3. (a) Amplitude variation with back-azimuth of P-to-S converted phase from dipping interfaces at different dip angles, (b) maximum amplitude variation with velocity contract across the dipping interface at different dip angles. The S-wave velocity differences are from 0.3 to 0.8 km/s correspond to S-wave velocity contrasts of 3.4/3.1, 3.5/3.1, 3.5/3.0, 3.6/3.0, 3.6/2.9, and 3.6/2.8 across the interface. Teleseismic ray parameter is 0.068 s/km.

Fig 3

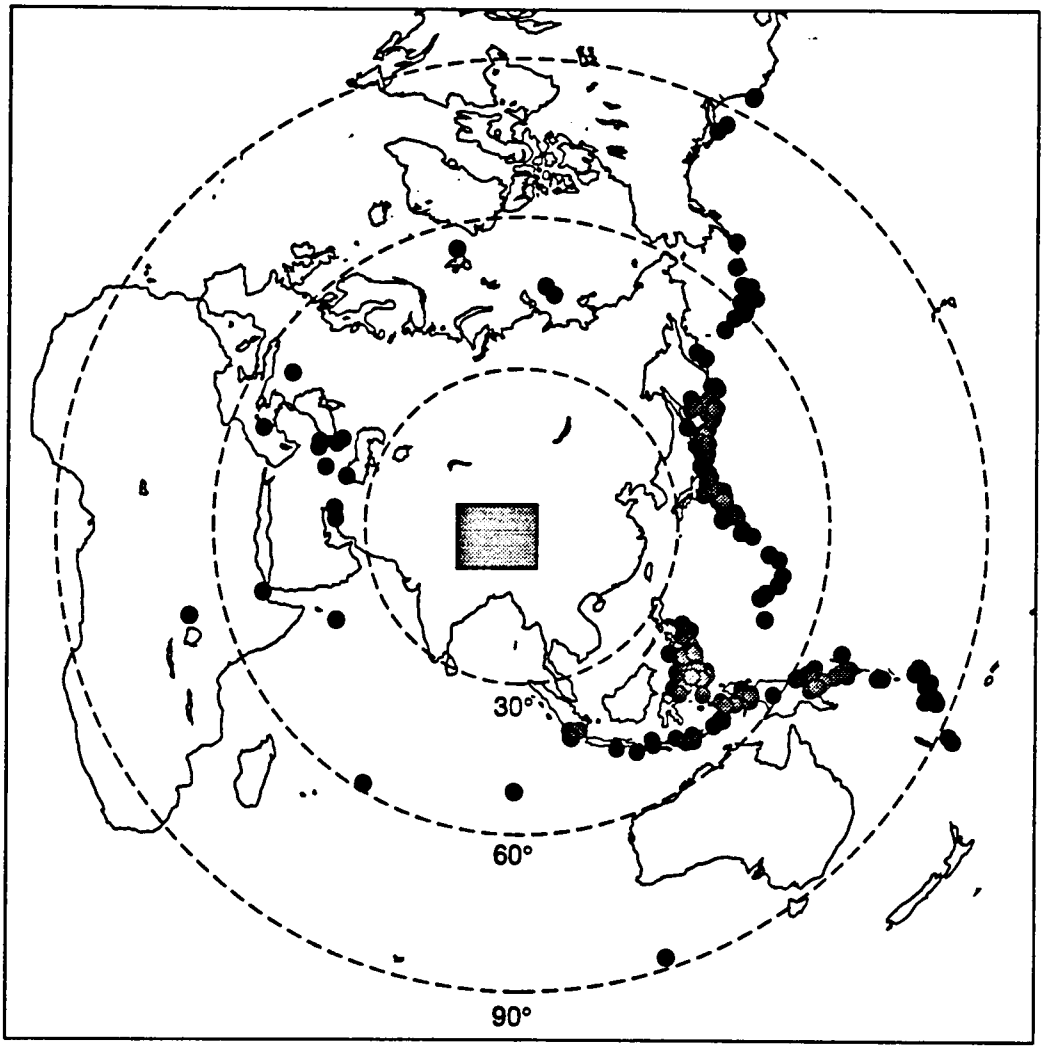

Figure 4. Teleseismic events used in this receiver function study, their epicentral distances range from 35° to 95° with respect to station BUDO. The area in figure 1 is shown as gray box in the figure.

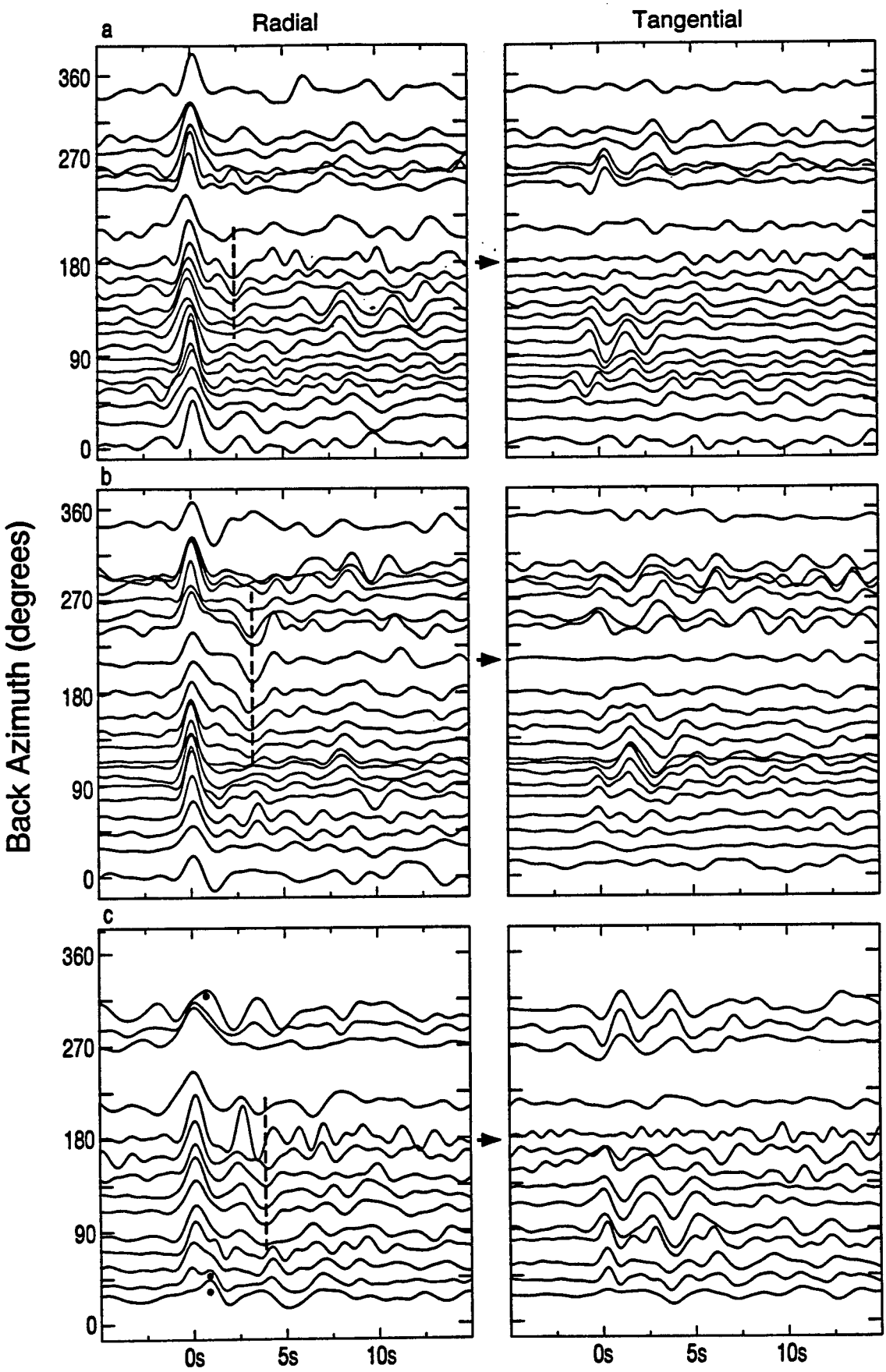

Figure 5. Variation of receiver functions with back-azimuth in station (a) TUNL, (b) BUDO, and (c) ERDO. Arrows point to the back-azimuth with minimum tangential energy. Also indicated by blackened dots are mid-crust P-to-S converted phases.

Fig 5

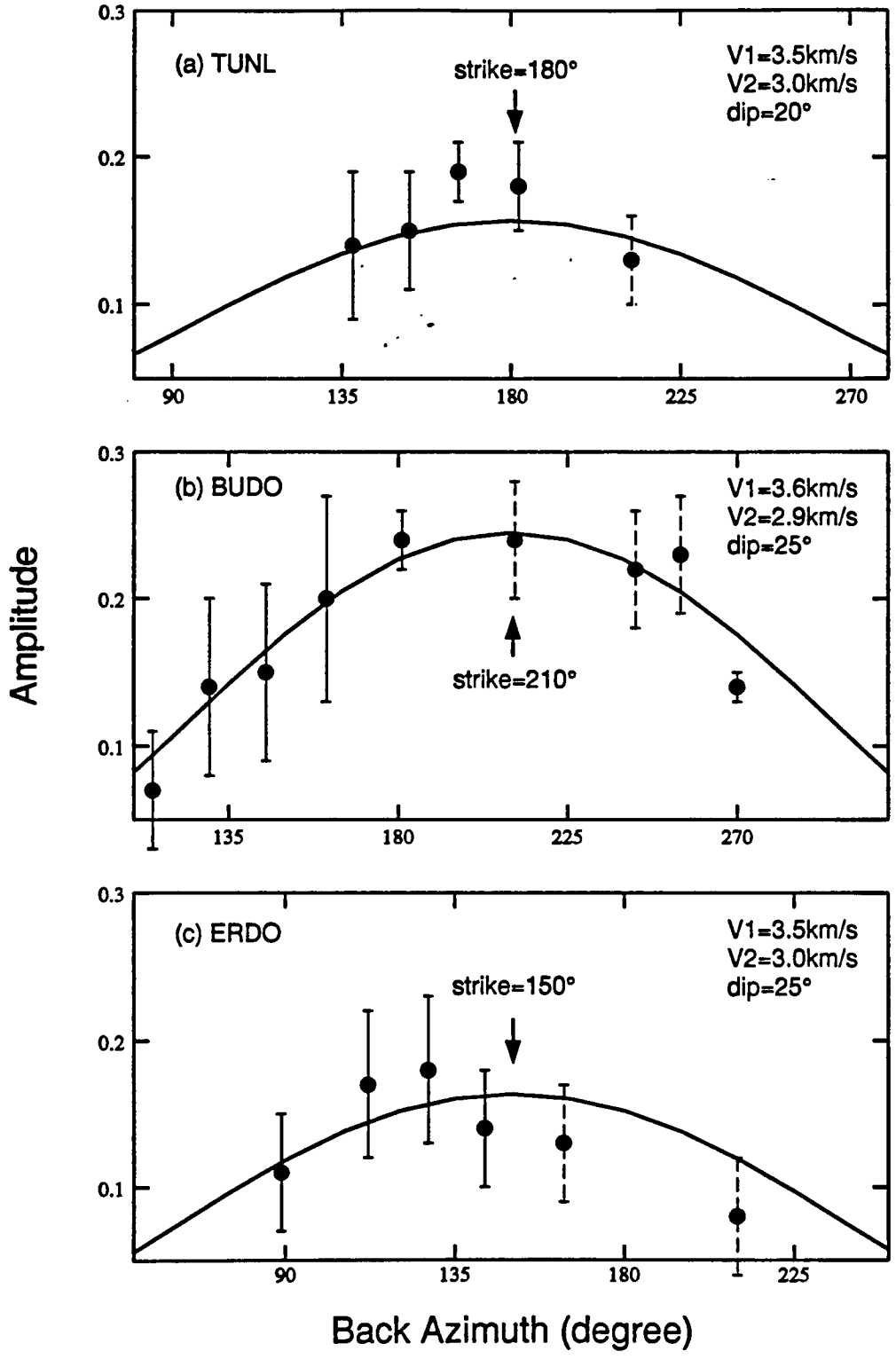

Figure 6. Measured absolute amplitudes of the mid-crust converted phases at three stations. Dashed error bar means only one event is available in this stacking suite so average standard deviation of other stacking suites is used. Solid line are synthetic calculations with the velocity contrast and dip angle shown in the figure.

Fig.6

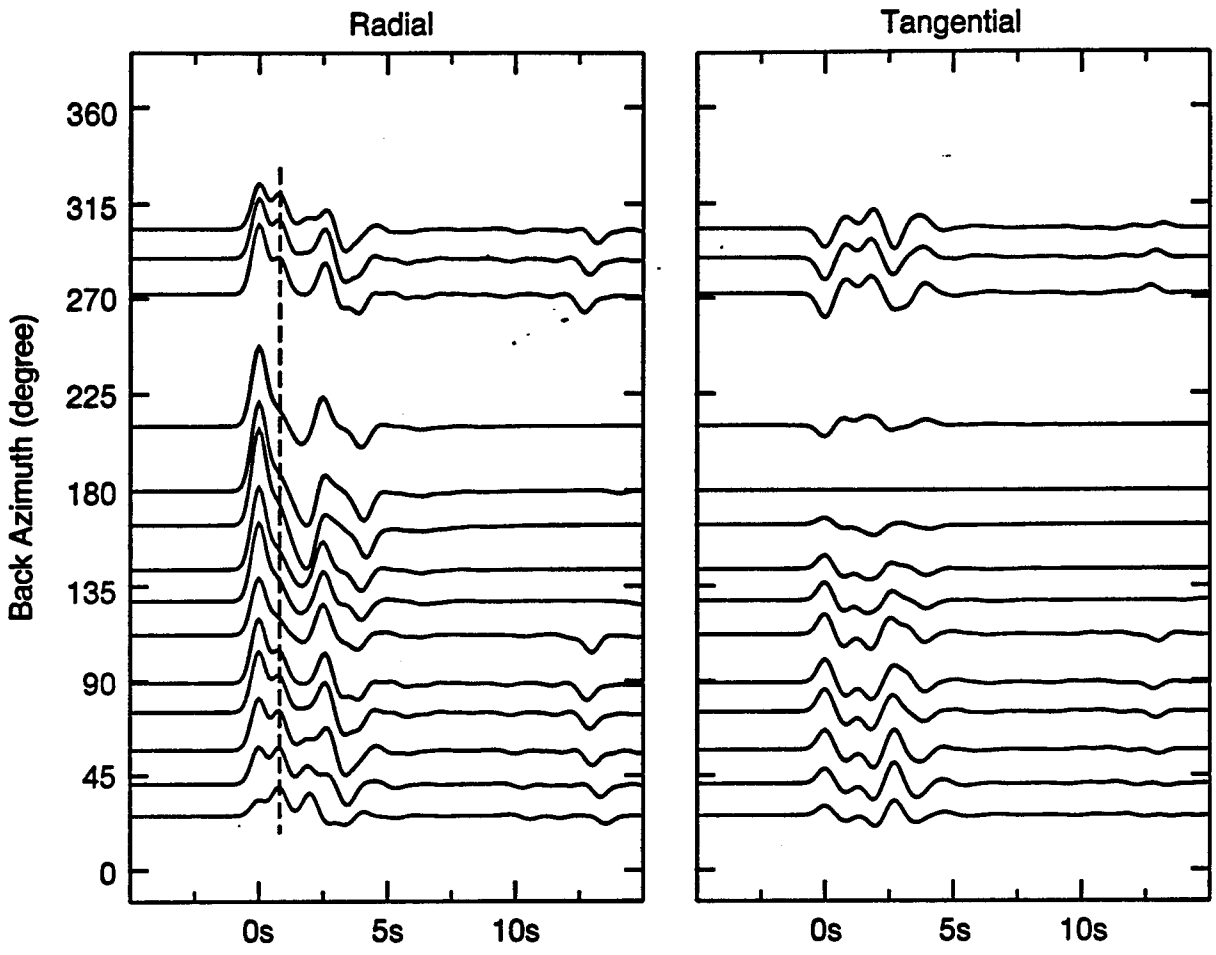

Figure 7. Synthetic receiver functions showing the effect of shallow dipping interface under ERDO. Dashed line indicats the Ps phase from the dipping interface (see paper).

Fig 7

Regional Earthquake Waveform Modeling on the Tibetan Plateau

L. Zhu and D. V. Helmberger

California Institute of Technology
Contract No. F49620-92-J-0470

OBJECTIVE

Broadband records of regional earthquakes can help to constrain the source mechanisms and crustal structure. The objective of this report is to study the crustal structure and source mechanisms by using regional earthquake waveform data obtained during the 1991-1992 passive recording experiment on the Tibetan Plateau (Owens et al., 1993). The data also provide an opportunity to test the ability of determining source mechanisms of regional events by broadband waveform modeling in an area where only limited number of stations are available and the structure is not well known.

RESEARCH ACCOMPLISHED

Introduction

The Tibet Plateau, produced by collision of two continental plates, India and Eurasia, has been a challenge in Earth science for a long time. Several models of collision and formation of the plateau have been proposed. But none of them can give a satisfactory explanation.

Seismic velocity structure of the crust and upper mantle can provide us information on the present state deep in the plateau, which is crucial to understanding the process of plateau formation. Due to the difficulties of accessing this area, previous seismic studies had to rely on the data recorded at stations outside the plateau. Most studies were done by using long-period surface wave, short-period travel time analysis, or waveform modeling (S, SS etc), see Zhao et al (1991). In 1991-1992, a passive source seismic recording experiment was conducted on the Tibet Plateau by Sino-US seismologists. For the first time, 11 digital broadband seismic stations were deployed on the plateau (Figure 1). Large amount of data was obtained from teleseismic and regional events.

In this report, we will use the data from several regional events to study the source mechanisms and the crustal structure. Two previous velocity models are examined and a new model is formed from the waveform modeling. We will also test the ability of of constraining the source mechanisms of regional events by one or few broadband stations.

Relocation of events and Pn, Sn velocities

More than 50 regional events with reasonable signal/noise ratio have been recorded during the one year experiment. We selected 5 events with 4 of them located within the array (Figure 1). Due to lack of reports of regional seismic stations and the difference of Tibet crust structure from standard earth model, the source location parameters of the events in Tibet give by PDE are not satisfactory. Thus, we first relocate the events by their first arrivals. The velocity model for relocation is a two-layer crust model simplified from previous teleseismic receiver function study (Zhu, 1993). It has a 3 km top layer with P velocity 4.5 km/s and 62 km layer with P velocity of 6.2 km/s, the uppermost mantle velocity is 8.1 km/s. Since most earthquakes in Tibet occur at depths between 5 to 20 km (Molnar and Chen, 1983; Zhao and Helmberger 1991), we fix the source depth at 10 km. The relocation results are listed in Table 1. It is shown that PDE tends to give later origin times for events in Tibet plateau because the

crust thickness used by PDE is much less than 65 km average thickness of Tibet crust.

Table 1 Event list and relocation results

Event	PDE origin time yr-mo-da hr mi t0	lat. °	long. °	h km	Mb	rms s	Relocation t0 s	lat. °	long. °	rms s	Δt0 s	Δx km
222	91-08-10 20 21 51.7	33.91	92.16	10	4.7	1.2	52.1	33.92	92.28	0.9	0.4	11
323	91-11-19 01 04 18.0	32.48	93.59	33	4.9	3.0	15.9	32.55	93.82	0.8	-2.1	23
330	91-11-26 21 15 59.9	34.07	94.25	33	4.3	2.5	57.6	34.09	94.23	0.8	-2.3	3
336	91-12-02 19 45 36.6	32.09	94.69	*	4.4	4.0	33.6	32.17	94.62	0.7	-3.0	11
348	91-12-14 08 20 23.8	33.98	88.84	33	5.1	5.4	20.8	33.93	89.06	0.3	-3.0	20

Event 222 was recorded by all the 11 stations in epicentral distance range of 80-800 km. In addition, it occurred in the middle of the north-south station line, forming a nature seismic profile. Figure 2 is a record section of this event. By identifying the Pn and Sn arrivals and using least-square fitting, we obtain the following travel time relations:

$$Pn = 12.39+\Delta/8.11 \quad (sec)$$

$$Sn = 23.90+\Delta/4.71 \quad (sec)$$

Our 8.11 km/s and 4.71 km/s for P and S velocities in uppermost mantle are very consistent with previous results (Chen and Molnar, 1981) The average crust P and S velocities estimated from intercept time are 3.46 km/s and 6.24 km/s, assuming the source depth of 10 km and crust thickness of 65 km. All these velocity analyses, combined with results of previous work, provide initial models for our next step involving waveform modeling.

Waveform modeling

To estimate the source mechanisms, we used a procedure developed by Zhao and Helmberger (1994). It uses a direct grid search in the strike, dip, rake and source depth parameter space for the minimum L1 and L2 norms of the difference between waveforms and synthetics. The method desensitizes the timing between principal crustal arrivals by fitting portions of the waveforms independently, allowing some time shifts between the observation and synthetics. We find that introducing one more parameter, the scalar moment, in the search process and using the same moment for all stations and components increases the resolution.

Two previous velocity models of Tibet plateau have been examined. Model M45 was derived from pure path phase velocity dispersions of long-period surface wave (Romanowicz, 1982). Another model, TIB, was from waveform modeling of regional long-period Love wave (Zhao et al., 1991). Figure 3 shows these two models. Both models give reasonably good waveform fits of the Love waves. But it turns out that TIB yields SmS arrivals that are too fast relative to the observed SmS (Figure 4). M45's prediction of SmS arrival times is better than TIB's. By comparing these two model, we conclude that TIB has mid-lower crustal velocities that are too high. This conclusion is also consistent with previous receiver function study (Zhu, 1993).

We start with a simple initial model: a low velocity top layer on a uniform crustal layer of 50 km thick with a transition zone above moho. By adjusting the thickness and velocities of each layer, we try to model the observed waveforms of both Pnl and surface wave. Generally, the Love wave provides constraint on the velocity structure of upper crust and Pnl, SmS provide constraint on the lower crust. Our final model is given in Figure 3 labeled T91: the top layer thickness is 3 km with a S velocity of 2.50 km/s and a P velocity of 4.45 km/s followed by a 50 km main crust with a S velocity of 3.45 km/s and a P velocity of 6.2 km/s. Moho is at a depth of 68 km with a 15 km transition zone above it. Figure 5 is the waveform fit by this model. For all 5 events, this model produces good fits between observations and synthetics, especially the SH components. The obtained source mechanisms are listed in Table 2. The two northern events are strike-slip type. The other 3 are normal fault type (Figure 1).

Table 2 Source mechanisms from waveform modeling

ent	whole array strike	dip	rake	M0 10^{22} dyn cm	depth km	error	one station (AMDO) strike	dip	rake	M0 10^{22} dyn cm	depth km	error
222	340	70	170	20.0	10	3.7	340	80	170	21.0	10	3.2
323	190	50	260	1.5	10	4.0	170	50	220	1.8	10	3.1
330	30	60	210	7.3	10	4.2	30	80	240	8.8	10	3.4
336	170	30	220	2.6	10	4.1	210	30	260	2.3	10	3.3
348	0	60	240	19.0	5	4.0	190	70	220	20.0	10	3.3

CONCLUSION AND RECOMMENDATIONS

The result of regional earthquake waveform modeling shows that the crust of Tibet plateau is roughly vertically uniform and has a very low average velocity, especially the shear velocity. It suggests that the temperature in the mid-lower crust is high which might be caused by the concentration of continental crust materials or high heat flow from the upper mantle. Our results are consistent with previous surface wave and teleseismic receiver function studies. Two types of source mechanisms have been obtained for 5 regional events: strike-slip with one EW-striking fault plane and normal fault with EW T-axes. The source mechanisms and their indicated stress states support the proposed EW extrusion and extension of the crust in the high plateau under the indentation of India subcontinent (Molar and Layon-Caen, 1989).

To test the ability of constraining source mechanism of regional events by one or few broadband stations, we select one station (AMDO) and only use its recordings to search for the source mechanisms. The solutions are also listed in Table 2 with solutions from the whole array. The result is encouraging. Under the circumstance that we have good Pnl and surface wave recordings and suitable velocity model, the source mechanisms can be obtained by one station, as found in California (Dreger and Helmberger, 1993). We believe such kind of test is very helpful for further broadband waveform modeling in area as Tibet where only few stations are available. For example, beginning from 1992 CDSN has one more permanent broadband station operating at Lhasa. More regional earthquake data can be accumulated in recent future.

References

Dreger, D. S. and D. V. Helmberger, 1993, Determination of source parameters at regional distances with three-component sparse network data, *J. Geophys. Res.* 98, 8107-8125.

Molnar P. and W. Chen, 1983, Focal depths and fault plane solution of earthquakes under the Tibetan Plateau. *J. Geophys. Res.* 88, 1180-1196.

Owens, T. J., G. E. Randall, F. T. Wu and R. S. Zeng, 1993, PASSCAL instrument performance during the Tibetan plateau passive seismic experiment, *Bull. Seism. Soc. Am. 83, 1959-1970.*

Romanowicz, B. A., 1982, Constraints on the structure of the Tibet Plateau from pure path phase velocities of Love and Rayleigh waves, *J. Geophys. Res.* 87, 6865-6883.

Zhao, L. and D. V. Helmberger, 1991, Geophysical implication from relocation of Tibetan earthquakes - hot lithosphere, *Geophys. Res. Lett.*, 18, 2205-2208.

Zhao, L., D. V. Helmberger, and D. G. Harkrider, 1991, Shear-velocity structure of the crust and upper mantle beneath the Tibetan and southeastern China, *Geophys. J. Int.* 105, 713-730.

Zhao, L. and D. V. Helmberger, 1994, Source estimation from broadband regional seismograms, *BSSA* 84, 91-104.

Zhu, L., R. S. Zeng, F. T. Wu, T. J. Owens, and G. E. Randall, 1993, Preliminary study of crust-upper mantle structure of the Tibetan Plateau by using broadband teleseismic body waveforms, *Acta Seism. Sinica* 6, 305-315.

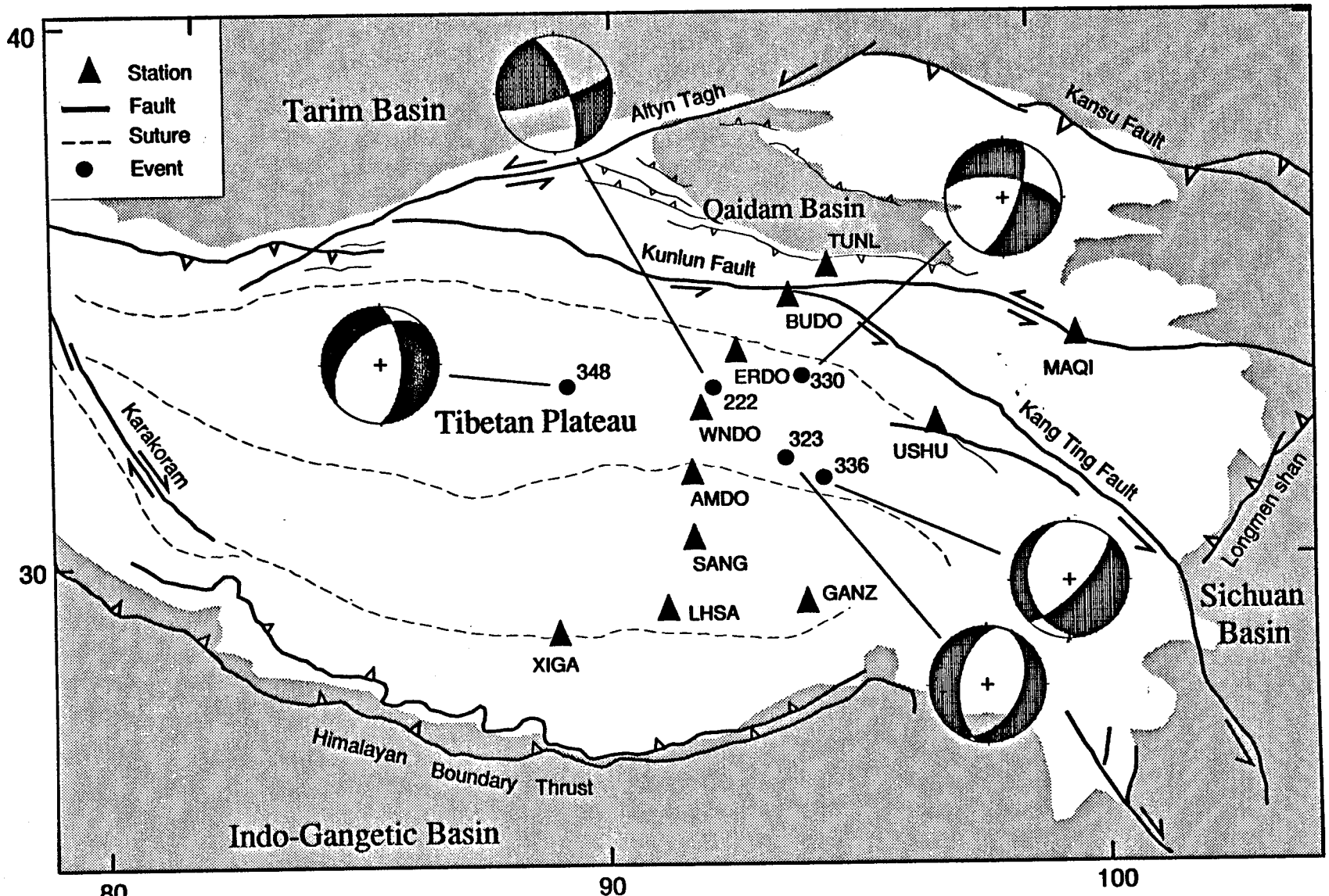

Fig.1 Tectonic sketch map of Tibet plateau (modified from Dewey et al., 1988), gray areas are below 3 km elevation. Blacken dots are 5 events with their source mechanisms from waveform modeling

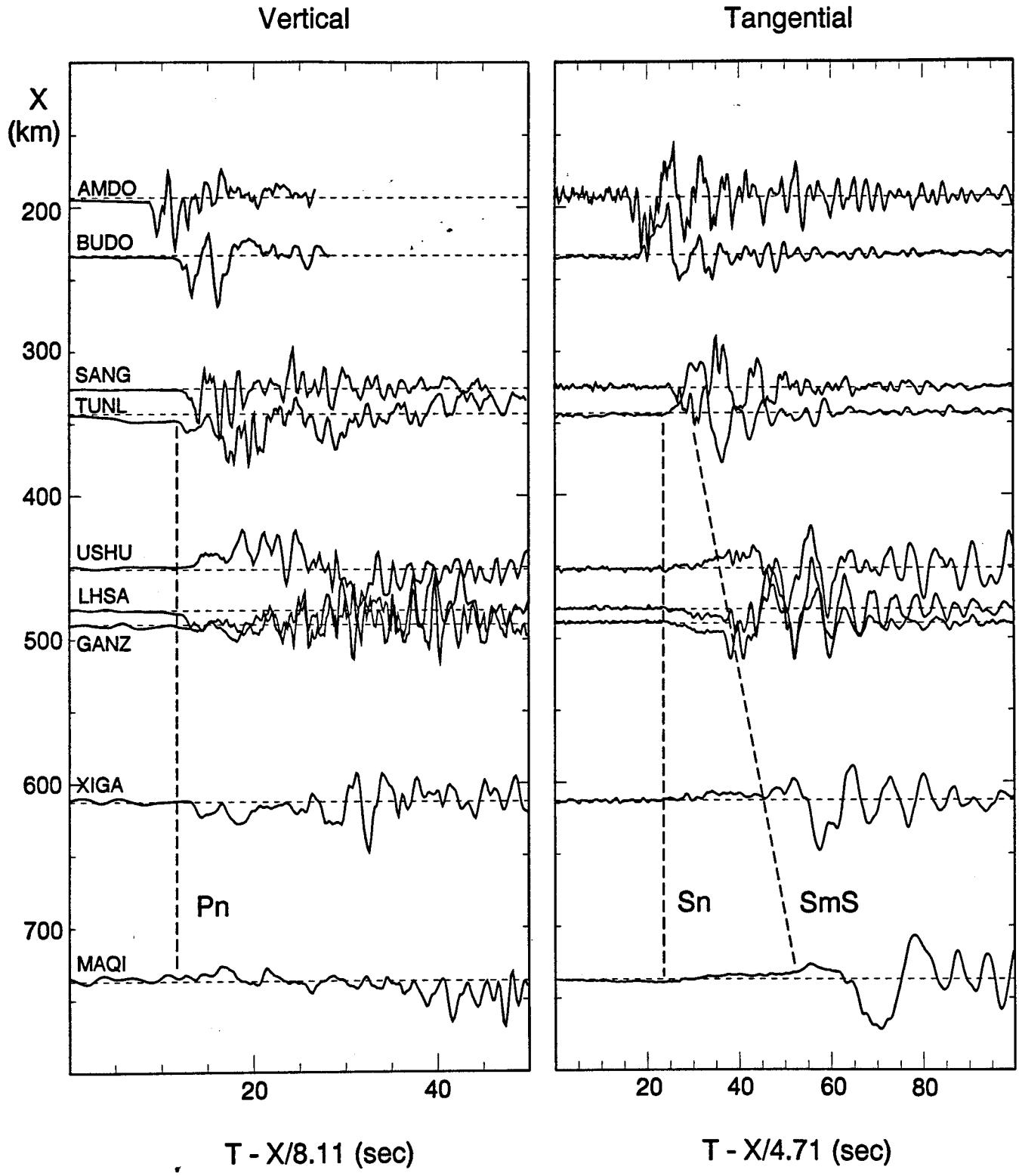

Fig. 2 Recording section of event 222, dashed lines show the Pn, Sn and SmS.

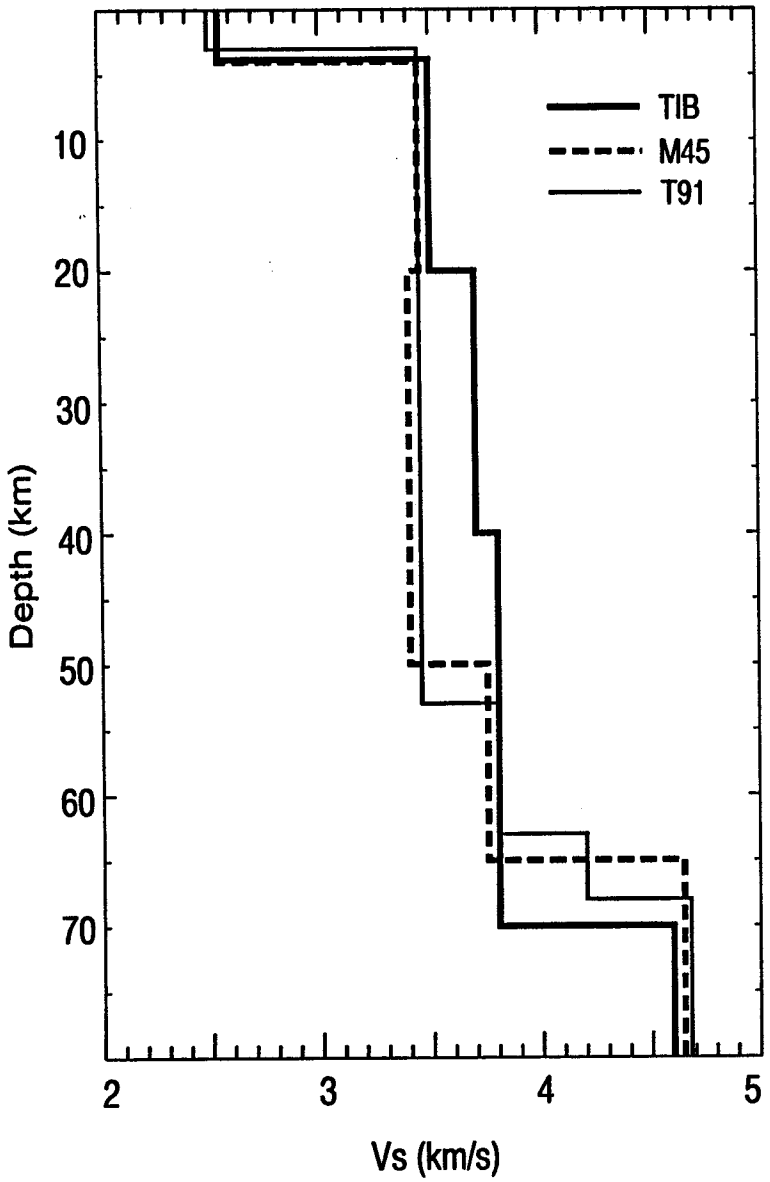

Fig.3 Model M45, TIB and T91 (see paper)

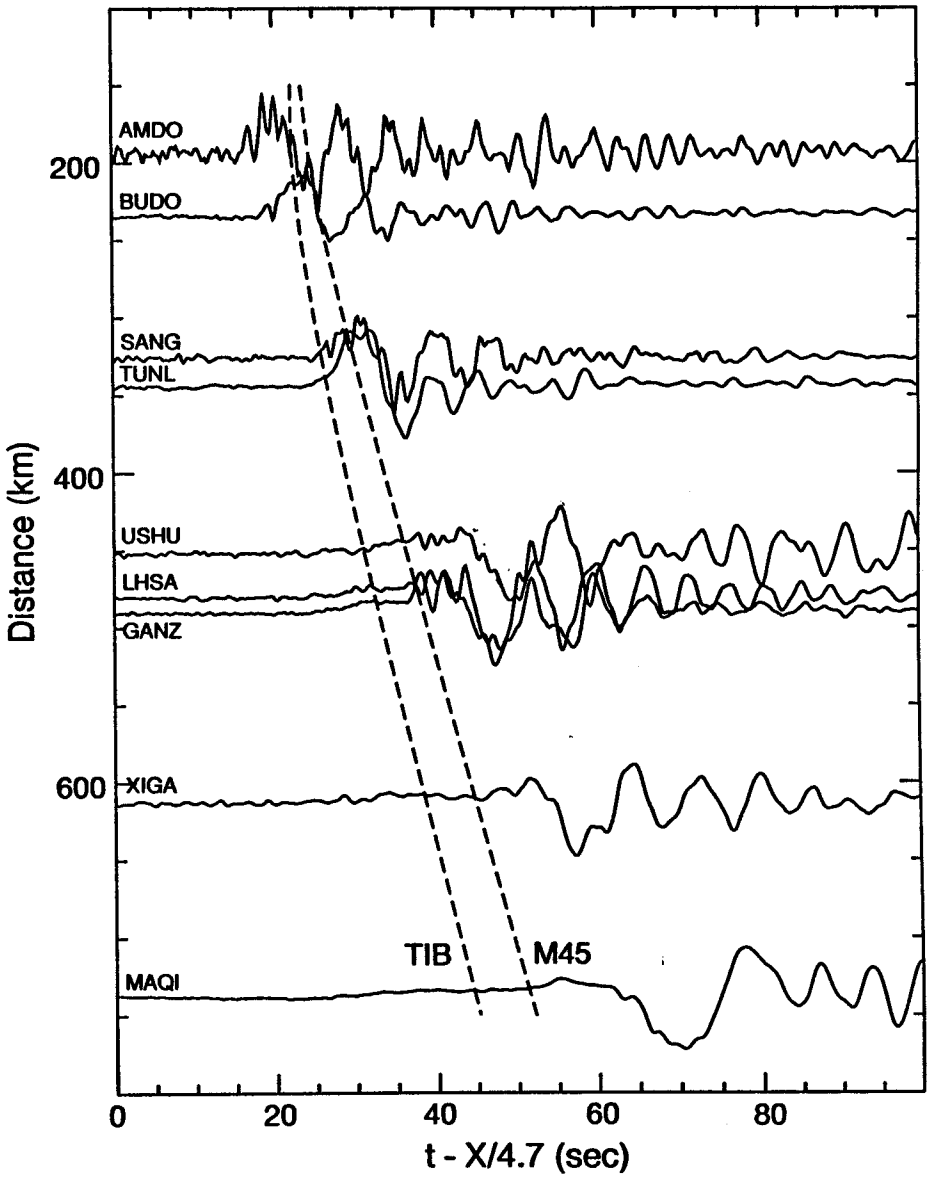

Fig.4 Polarity-corrected SH component record section of Event 222 and SmS arrival times predicted by model TIB and M45

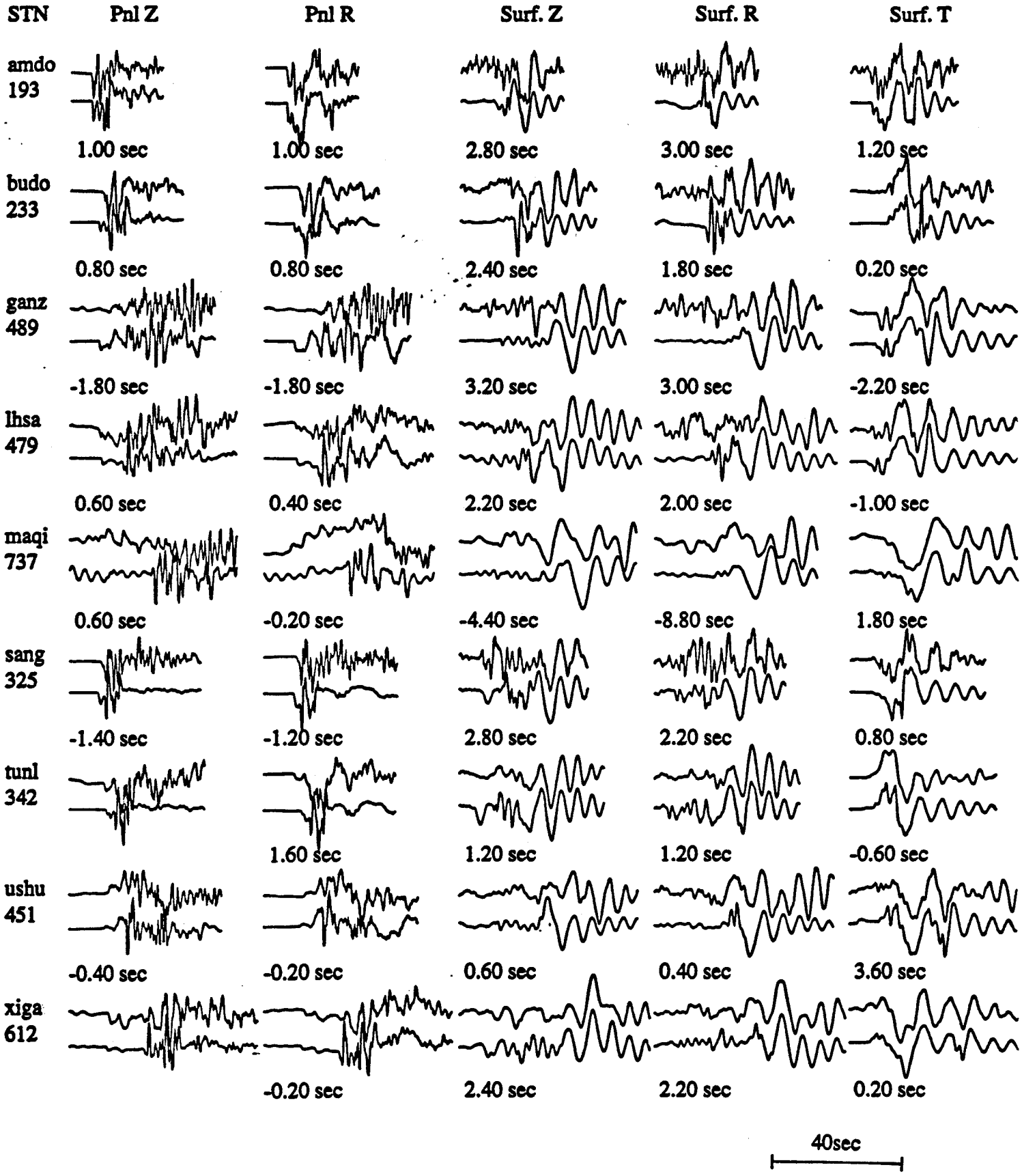

Fig. 5a Waveform modeling of Event *222*, upper traces are observation and lower traces are synthetics with time shifts in sec (positive number means synthetic is shifted back). Numbers below station names are distances in km. Model used is T91 with source at depth of 10 km. Source mechanism from modeling is strike 340, dip 70, rake 170, and moment 2.0 x 10^{23} dyn. cm error 3.7

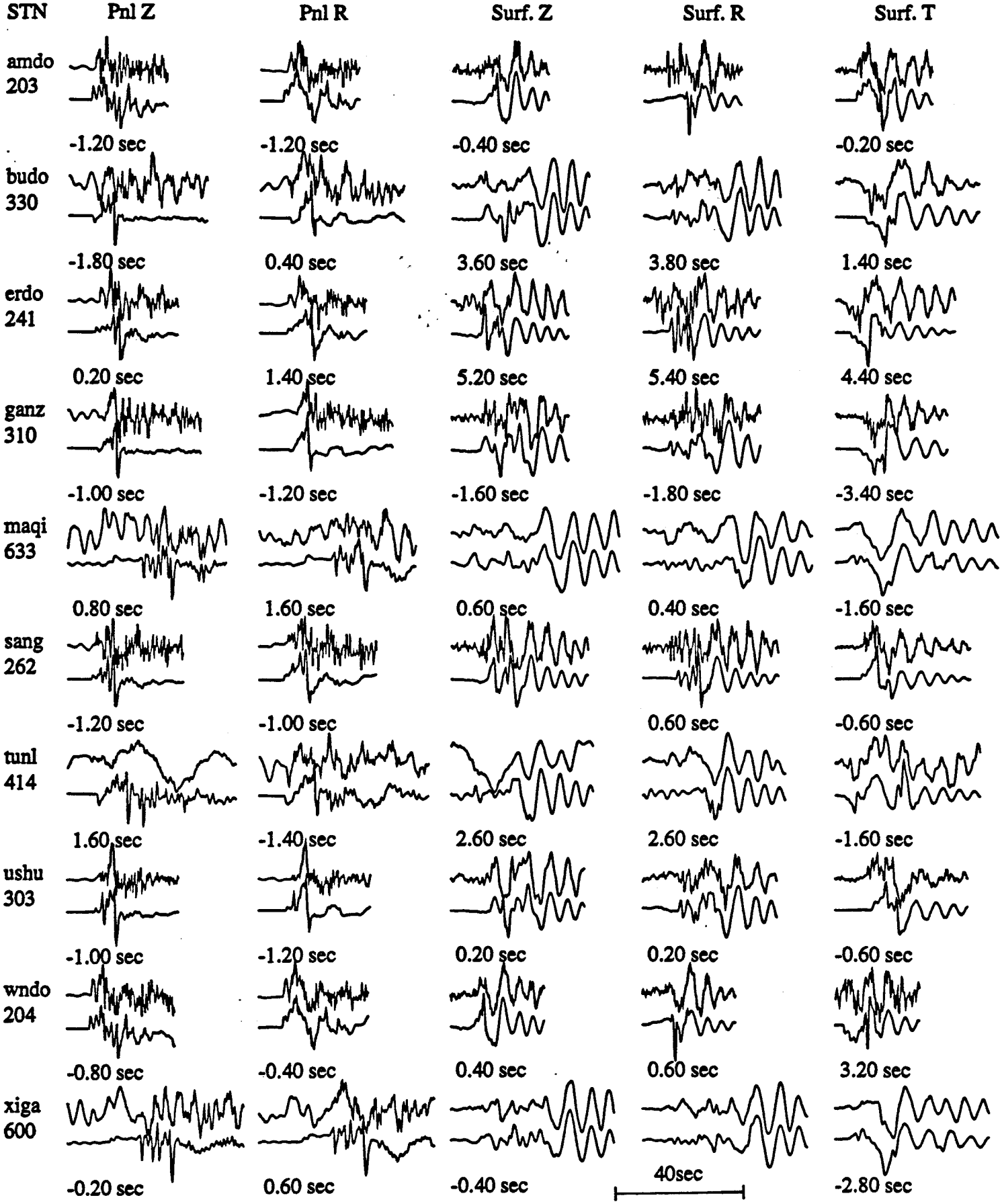

Fig. 5b Waveform modeling of Event *323*, upper traces are observation and lower traces are synthetics with time shifts in sec (positive number means synthetic is shifted back). Numbers below station names are distances in km. Model used is T91 with source at depth of 10 km. Source mechanism from modeling is strike 190, dip 50, rake 260, and moment 1.5 x 10^{22} dyn. cm error 4.0

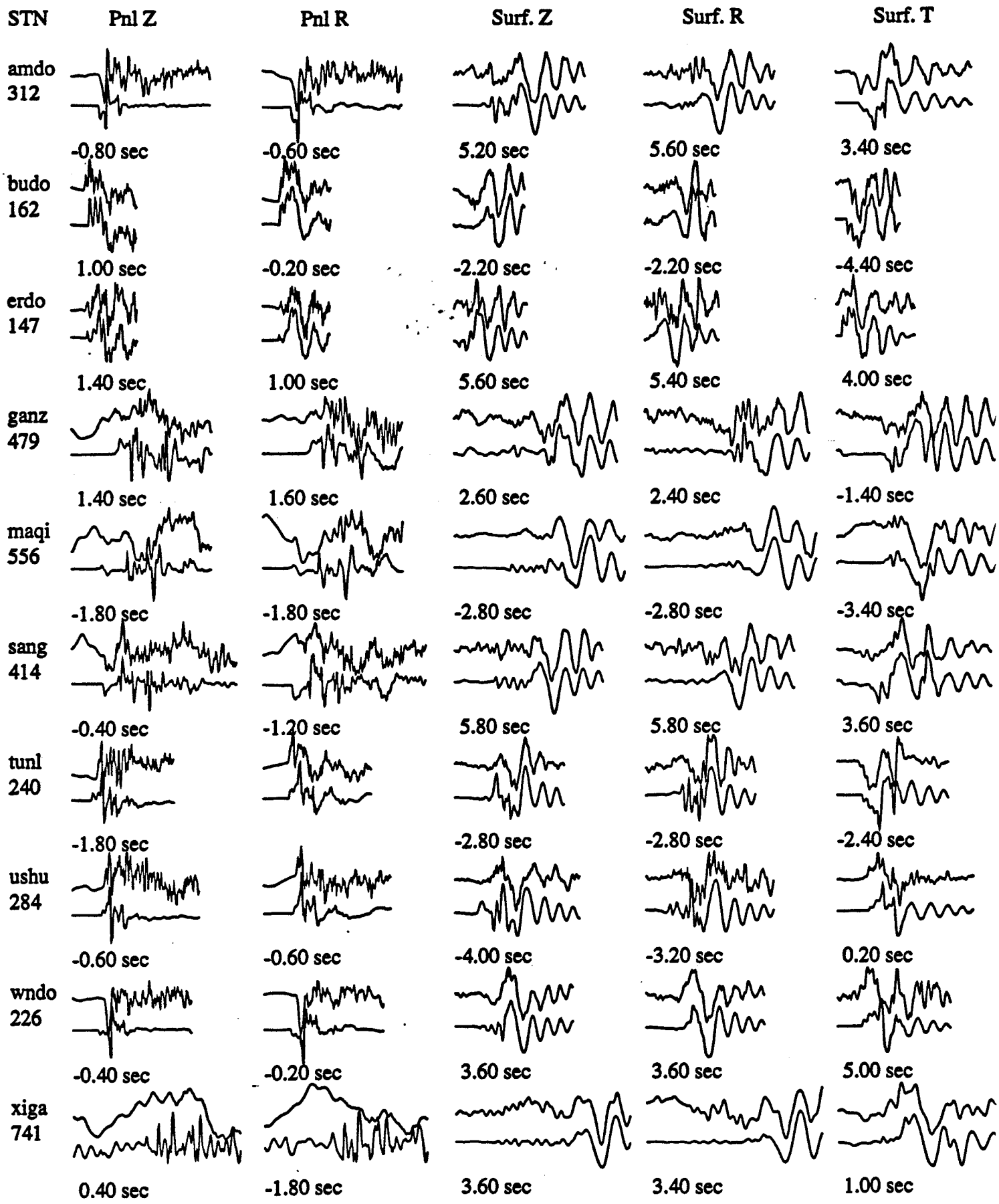

Fig. 5c Waveform modeling of Event ***330***, upper traces are observation and lower traces are synthetics with time shifts in sec (positive number means synthetic is shifted back). Numbers below station names are distances in km. Model used is T91 with source at depth of 10 km. Source mechanism from modeling is strike 30, dip 60, rake 210, and moment 7.3 x 10^{22} dyn. cm error 4.2

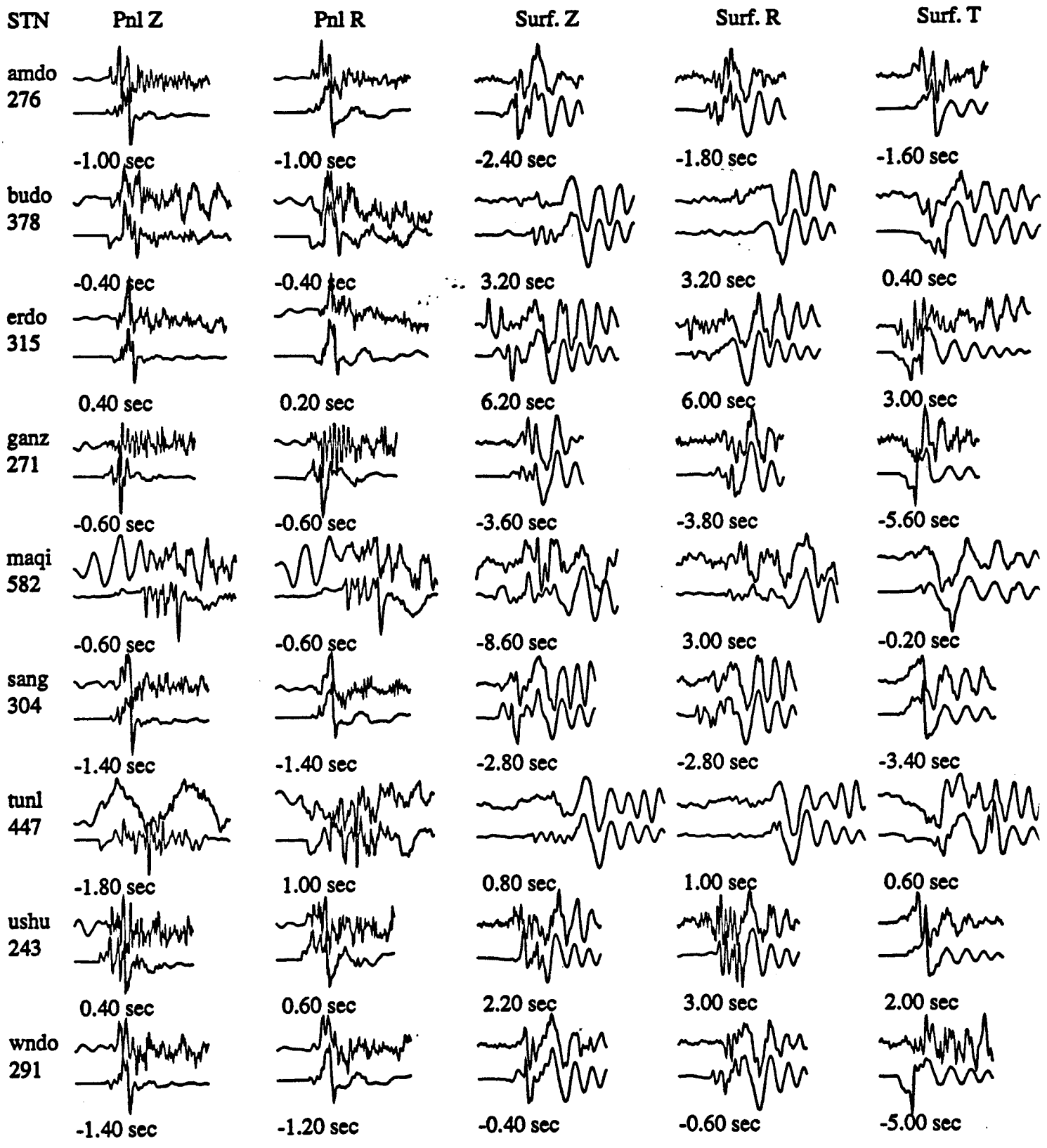

Fig. 5d Waveform modeling of Event *336*, upper traces are observation and lower traces are synthetics with time shifts in sec (positive number means synthetic is shifted back). Numbers below station names are distances in km. Model used is T91 with source at depth of 10 km. Source mechanism from modeling is strike 170, dip 30, rake 220, and moment 2.6 x 10^{22} dyn. cm error 4.1

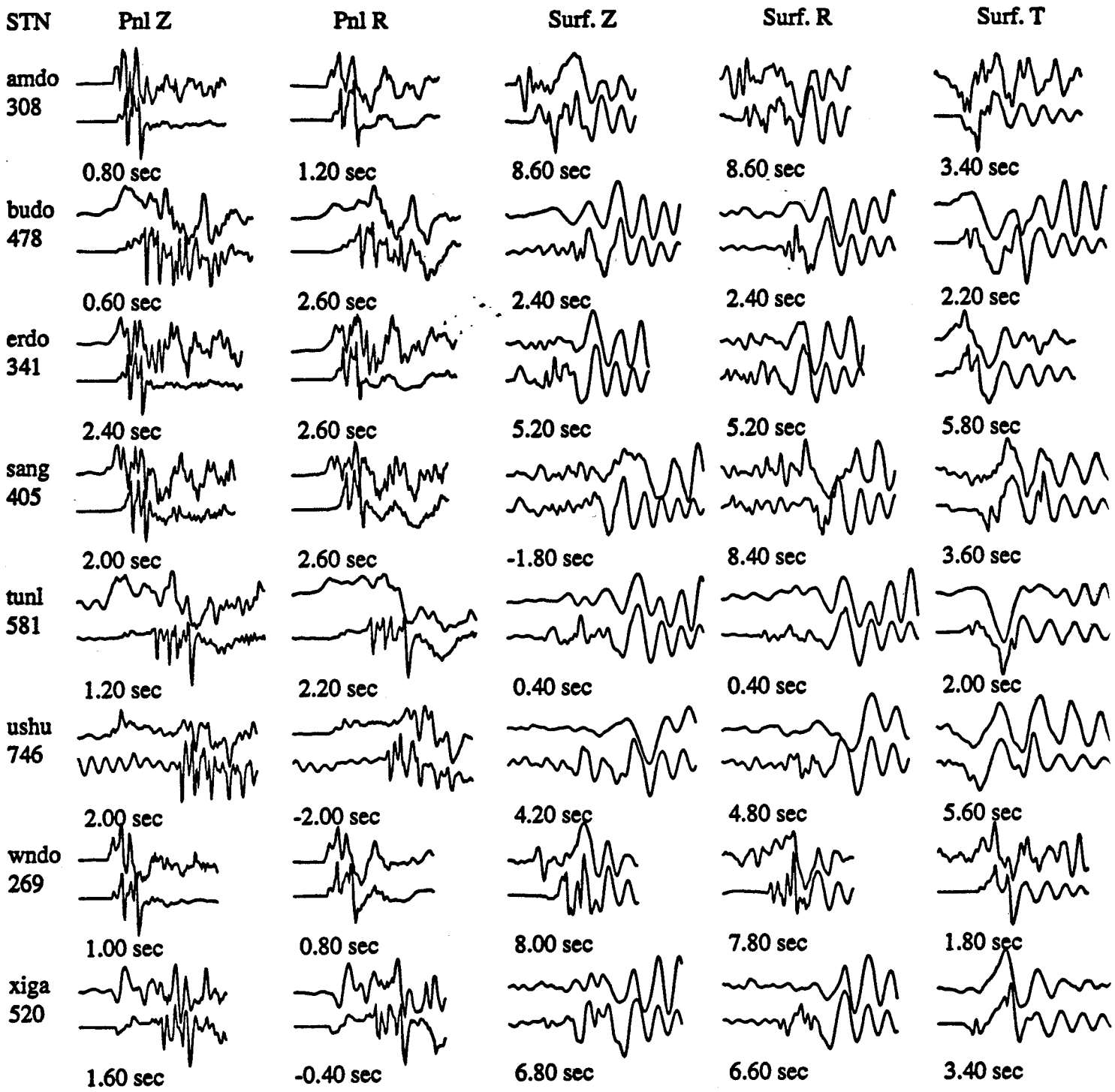

Fig. 5e Waveform modeling of Event *348*, upper traces are observation and lower traces are synthetics with time shifts in sec (positive number means synthetic is shifted back). Numbers below station names are distances in km. Model used is T91 with source at depth of 10 km. Source mechanism from modeling is strike 10, dip 50, rake 250, and moment 2.0×10^{23} dyn. cm error 4.0